Molecular Cell

Article

# An IDR-dependent mechanism for nuclear receptor control of Mediator interaction with RNA polymerase II

## Graphical abstract

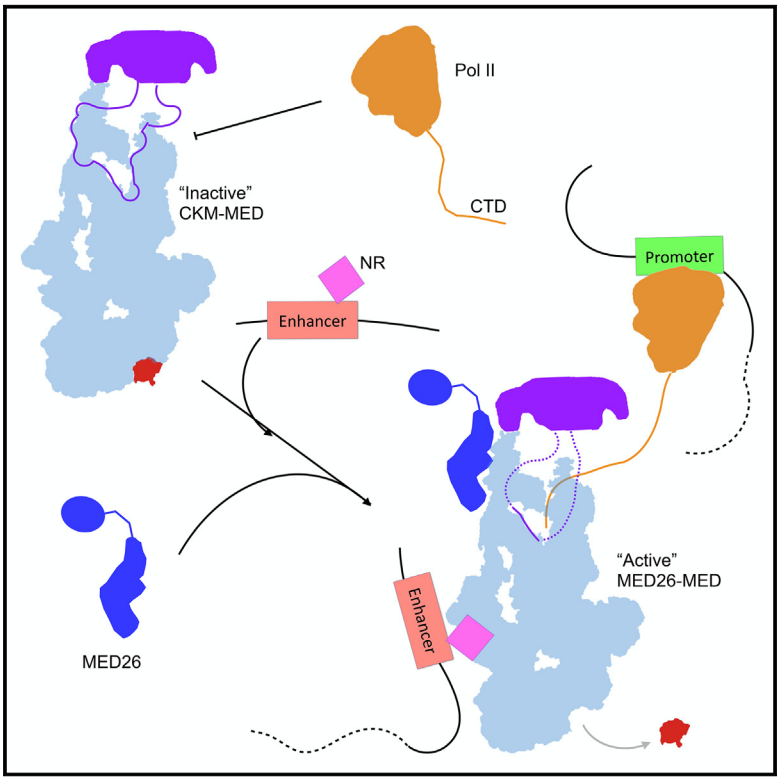


## Authors

Haiyan Zhao, Jiaqin Li, Yufei Xiang, ..., Yi Shi, Rafael Casellas, Francisco J. Asturias

## Correspondence

francisco.asturias@cuanschutz.edu

## In brief

Zhao et al. report that MED26 and the CDK8 kinase module (CKM) competitively bind Mediator (MED), modulating its interaction with RNA polymerase II (RNA Pol II). Preferential binding of nuclear receptors to CKM-MED, which cannot bind RNA Pol II, enables CKM exchange for MED26 and RNA Pol II interaction, resulting in transcription activation.

## Highlights

- MED26 and the CDK8 kinase module (CKM) compete for interaction with Mediator (MED)
- MED26-MED can bind RNA Pol II whereas CKM-MED, targeted by nuclear receptors (NRs), cannot
- NR binding to CKM-MED enables CKM exchange for MED26 and RNA Pol II interaction
- Transcription activation by NRs hinges on modulation of RNA Pol II binding to CKM-MED

Zhao et al., 2024, Molecular Cell *84*, 1–17
July 25, 2024 
https://doi.org/10.1016/j.molcel.2024.06.006

CellPress

Please cite this article in press as: Zhao et al., An IDR-dependent mechanism for nuclear receptor control of Mediator interaction with RNA polymerase II, Molecular Cell (2024), https://doi.org/10.1016/j.molcel.2024.06.006

Molecular Cell

CellPress

Article

# An IDR-dependent mechanism for nuclear receptor control of Mediator interaction with RNA polymerase II

Haiyan Zhao,[1,10] Jiaqin Li,[1,10] Yufei Xiang,[2] Sohail Malik,[3] Supriya V. Vartak,[4,7] Giovana M.B. Veronezi,[1] Natalie Young,[1] McKayla Riney,[1] Jens Kalchschmidt,[4,7] Andrea Conte,[4,8] Seol Kyoung Jung,[5] Srinivas Ramachandran,[1,6] Robert G. Roeder,[3] Yi Shi,[2] Rafael Casellas,[4,9] and Francisco J. Asturias[1,11,*]

[1]Department of Biochemistry and Molecular Genetics, University of Colorado Anschutz Medical School, Aurora, CO 80045, USA
[2]Center of Protein Engineering and Therapeutics, Icahn School of Medicine at Mount Sinai, New York, NY 10029, USA
[3]Laboratory of Biochemistry and Molecular Biology, Rockefeller University, New York, NY 10065, USA
[4]Lymphocyte Nuclear Biology, NIAMS, NIH, Bethesda, MD 20892, USA
[5]Biodata Mining and Discovery Section, NIAMS, NIH, Bethesda, MD 20892, USA
[6]RNA Bioscience Initiative, University of Colorado Anschutz Medical School, Aurora, CO 80045, USA
[7]Present address: Genomics and Immunity Section, NIAMS, NIH, Bethesda, MD 20892, USA
[8]Present address: Department of Molecular Medicine and Medical Biotechnology, Università degli Studi di Napoli Federico II, Naples, Italy
[9]Present address: Hematopoietic Biology and Malignancy, The University of Texas MD Anderson Cancer Center, Houston, TX 77030, USA
[10]These authors contributed equally
[11]Lead contact
*Correspondence: francisco.asturias@cuanschutz.edu
https://doi.org/10.1016/j.molcel.2024.06.006

## SUMMARY

The essential Mediator (MED) coactivator complex plays a well-understood role in regulation of basal transcription in all eukaryotes, but the mechanism underlying its role in activator-dependent transcription remains unknown. We investigated modulation of metazoan MED interaction with RNA polymerase II (RNA Pol II) by antagonistic effects of the MED26 subunit and the CDK8 kinase module (CKM). Biochemical analysis of CKM-MED showed that the CKM blocks binding of the RNA Pol II carboxy-terminal domain (CTD), preventing RNA Pol II interaction. This restriction is eliminated by nuclear receptor (NR) binding to CKM-MED, which enables CTD binding in a MED26-dependent manner. Cryoelectron microscopy (cryo-EM) and cross-linking-mass spectrometry (XL-MS) revealed that the structural basis for modulation of CTD interaction with MED relates to a large intrinsically disordered region (IDR) in CKM subunit MED13 that blocks MED26 and CTD interaction with MED but is repositioned upon NR binding. Hence, NRs can control transcription initiation by priming CKM-MED for MED26-dependent RNA Pol II interaction.

## INTRODUCTION

Mediator (MED) is a large, conserved complex essential for basal and activated transcription in all eukaryotes.[1–3] MED comprises 26–30 subunits (depending on the species) organized into 4 modules: head, middle, tail, and the CDK8 kinase module (CKM).[4,5] Most MED proteins associate into a stable core MED (cMED) complex, organized around the large, central scaffolding protein MED14.[6–8] An important exception is the 4-protein CKM, which displays a dynamic association with cMED[9,10] and is generally thought to block interaction of RNA polymerase II (RNA Pol II) with cMED.

Cryoelectron microscopy (cryo-EM) maps and corresponding molecular models of yeast and mammalian MEDs and preinitiation complexes (PICs) have revealed MED undergoing conserved and well-defined conformational rearrangements that secure RNA Pol II and basal factors into a stable MED-PIC in which the TFIIH kinase responsible for phosphorylation of the RNA Pol II carboxy-terminal domain (CTD) is stabilized to engage its target.[8,11–13] These structures, however, have not provided any insight into how MED works in activated transcription, except for revealing that MED subunit domains targeted by activators are predominantly intrinsically disordered regions (IDRs).[14,15] It is hard to envision how activator binding to these IDRs could prompt structural changes in the well-ordered cMED, challenging a long-standing expectation that activator-initiated conformational rearrangements in MED might promote transcription activation.[9,16]

Previously, we used cryo-EM and RNA sequencing (RNA-seq) to examine the structural and transcriptional effect of single and multiple subunit deletions in mMED.[14] Deletion of MED1, which facilitates cMED conformational rearrangements,[14] affected the expression of only ~10% of genes. Unexpectedly, deletion of the metazoan-specific MED26, a small (65 kDa, or 4% of

Please cite this article in press as: Zhao et al., An IDR-dependent mechanism for nuclear receptor control of Mediator interaction with RNA polymerase II, Molecular Cell (2024), https://doi.org/10.1016/j.molcel.2024.06.006



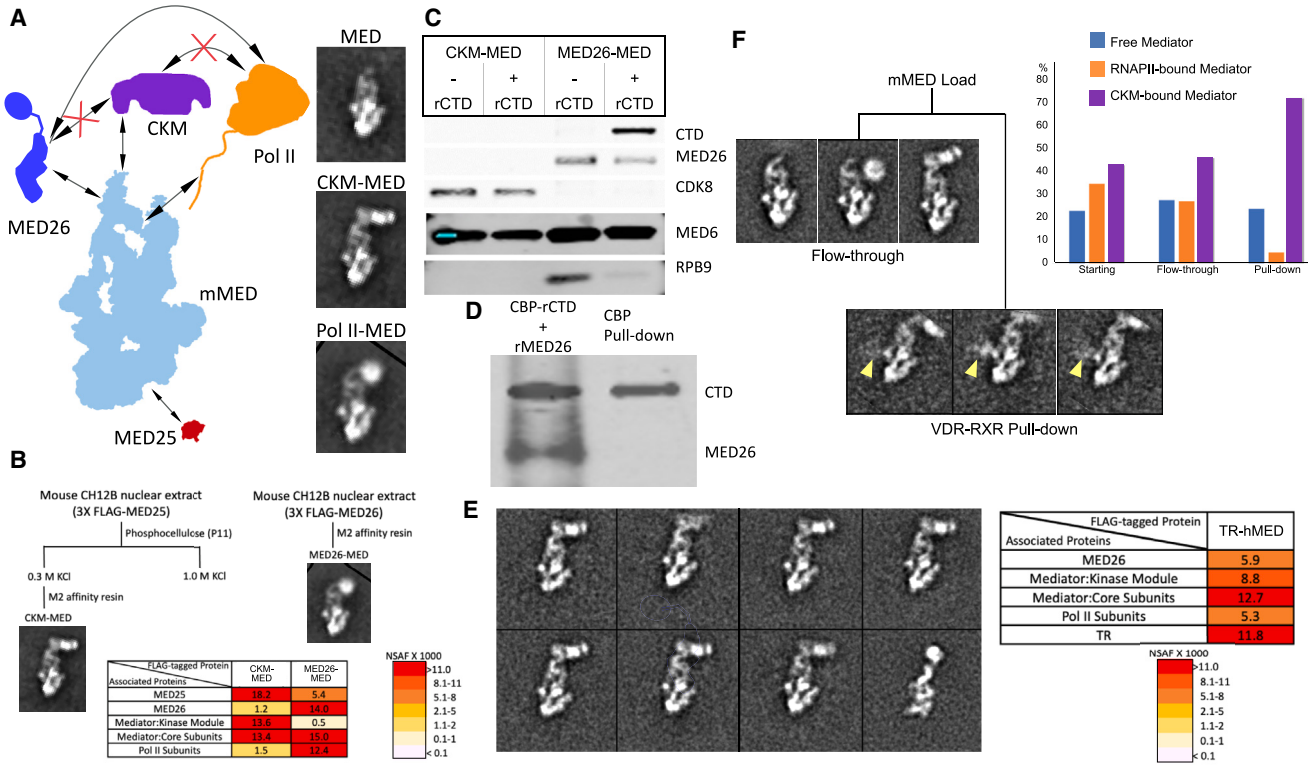


**Figure 1. Dynamic interaction of cMED with MED26, the CKM, and RNA Pol II *in vitro* and in a purified endogenous complex**

(A) Dynamic association of RNA Pol II and Mediator subunits (CKM and MED26) with cMED, and EM class averages of the different complexes.

(B) Strategy used to obtain MED26-MED and CKM-MED (see STAR Methods; CKM-MED was purified from the flowthrough of a P11 column [PC-FT]). The table shows MudPIT results for subunit composition of the two complexes.

(C) Interaction of MED26-MED and CKM-MED with recombinant CTD (rCTD) by western blotting. A representative gel is shown; each experiment was independently repeated three times. MED26-MED interacts with the CTD, apparently by exchanging bound RNA Pol II for recombinant CTD (note the decrease in intensity of the RPB9 band after CTD interaction). CKM-MED does not interact with CTD. For these experiments, MED26-MED and CKM-MED were immobilized through FLAG tags on MED26 and MED25, respectively (see STAR Methods).

(D) Recombinant full-length MED26 (rMED26) does not interact with rCTD directly *in vitro*. Recombinant CBP-tagged CTD was immobilized on calmodulin resin and incubated with recombinant MED26. After resin washes, bound complex was eluted and tested for the presence of MED26 by western blotting.

(E) 2D class averages calculated from images of TR-hMED particles preserved in stain showed that a majority of TR-hMED particles include the CKM. MudPIT analysis results confirm that TR-hMED includes near-stoichiometric amounts of CKM subunits and only small amounts of MED26 and RNA Pol II.

(F) EM analysis of a purified MED preparation before and after ligand-dependent interaction with an immobilized VDR-RXR-DNA-D3 complex through GST-tagged RXR. The purified MED load was a mixture, including comparable amounts of cMED, RNA Pol II-cMED, and CKM-MED. The flowthrough after incubation with the immobilized NR complex was also a mixture, but the elution was greatly enriched in CKM-MED. Nearly half of the eluted CKM-MED particles showed diffuse density near MED1 (yellow arrow heads), which was not detected in CKM-MED particles prior to interaction with the VDR complex, suggesting some ordering of the MED1 IDR upon NR interaction. See also Figure S1.

MED's total MW) dissociable subunit involved in recruitment of elongation factors[17] and loosely linked to increased cMED interaction with RNA Pol II,[10,18] had dramatic consequences, affecting ~50% of the transcriptome. The outsized effect of MED26 deletion, comparable to that resulting from simultaneous deletion of all major activator target tail subunits,[14] could not be explained by the cMED structure. An essential role for MED26 is evidenced by our previous observation that, although only a relatively small fraction of total MED in nuclear extracts is associated with MED26, quantitative immunodepletion of MED26 results in a nuclear extract that can support neither basal nor activated transcription.[19]

Several studies in yeast have focused on the effect of the CKM on RNA Pol II interaction with cMED and concluded that CKM physically prevents it,[20–22] with a recent report proposing that release of this inhibition requires CKM's CDK8 kinase activity.[23] However, the functional significance and underlying mechanism for opposite effects of MED26 and the CKM on mammalian cMED interaction with RNA Pol II (Figure 1A) are not understood. Here, we present results that provide a structural and mechanistic framework to understand how modulation of mMED interaction with RNA Pol II might link activators to control of transcription initiation.

## RESULTS

### Dynamic MED subunit association with cMED and effect on CTD binding

Electron microscope (EM) imaging following MED purification from nuclear extracts shows a combination of core, CKM-bound,

Please cite this article in press as: Zhao et al., An IDR-dependent mechanism for nuclear receptor control of Mediator interaction with RNA polymerase II, Molecular Cell (2024), https://doi.org/10.1016/j.molcel.2024.06.006



and RNA Pol II-bound MED, which are easily distinguishable owing to their known structures (Figure 1A). The relative abundance of each complex can be determined by "counting" MED particles in image subsets identified through two-dimensional (2D) classification.[14] RNA Pol II-MED appears almost exclusively as a complex in which RNA Pol II is tethered to cMED through the RNA Pol II CTD,[6,24] not as a fully formed "holoenzyme."[7,25] This is consistent with the CTD's essential role in RNA Pol II-MED complex formation,[24] and suggests that CTD-dependent tethering constitutes a critical initial step in RNA Pol II interaction with MED. To investigate how MED26 and the CKM might affect this initial step, we analyzed CTD binding to CKM-MED and MED26-MED complexes. We obtained pure, stoichiometric CKM-MED and MED26-MED through chromatographic and affinity purification protocols (Figure 1B, top). Multidimensional protein identification technology (MudPIT) characterization of the complexes showed that MED26-MED was stoichiometric on MED26 (the tagged subunit) and enriched in RNA Pol II, but was substoichiometric in MED25, and included only a minute amount of CKM subunits. In contrast, CKM-MED included stoichiometric amounts of MED25 (the tagged subunit) and CKM subunits, but only minute amounts of MED26 or RNA Pol II (Figure 1B, bottom).

Upon examining CTD association with MED26-MED and CKM-MED, we found that MED26-MED readily interacted with the CTD (Figures 1C right and S1A), consistent with previous, unexplained observations of enhanced RNA Pol II association with cMED in the presence of MED26.[10,18] Importantly, recombinant MED26 did not interact directly with the CTD *in vitro* (Figure 1D), indicating that MED26 does not physically engage the CTD but, instead, facilitates its interaction with cMED. In contrast, CKM-MED did not interact with the CTD (Figures 1C left and S1A). Previous studies[20–23] sought to explain why the CKM blocks interaction of RNA Pol II with cMED, but they focused on the polymerase and none revealed that CKM-MED cannot engage the CTD. Our results indicate that the opposite roles of MED26 and CKM on RNA Pol II-MED complex formation are explained by their opposite effects on the initial CTD engagement step.

## NR interaction with mMED complexes

Although one might expect an "active" form of MED to be recruited to regulatory elements, in yeast cells, the predominant form of MED at upstream activating sequences is CKM-MED.[26,27] Likewise, when metazoan MED is purified through affinity tagging of thyroid hormone or vitamin D nuclear receptors (NRs) that, in a ligand-dependent manner, interact tightly and very stably with the MED1 C-terminal IDR,[9,16,28–30] the resulting preparations are highly enriched in CKM-MED.[9,16,31] Therefore, we decided to examine the composition and interactions of NR-MED complexes. We used EM and MudPIT to examine the composition of TR-hMED (originally referred to as TR-TRAP[31]), a form of human MED complex purified from a HeLa-derived cell line ($\alpha$-2) that constitutively expresses a FLAG-tagged version of thyroid hormone receptor $\alpha$ (FLAG-TR$\alpha$).[28,29,31] We found TR-hMED to be present primarily as CKM-MED (65%–70%) (Figures 1E and S1B). To investigate the interaction of various mMED forms with NRs *in vitro*, we immobilized recombinant GST-tagged retinoid X receptor (RXR) in complex with vitamin D receptor (VDR) and its cognate DNA in the presence of ligand ($D_3$), and incubated it with a mMED preparation purified through a FLAG tag on MED25. EM analysis of the mMED preparation prior to interaction with the immobilized VDR complex revealed the usual mixture of core, CKM-bound, and RNA Pol II-bound MED (Figure 1F, left). In contrast, EM analysis of the fraction eluted after interaction with the immobilized VDR complex showed enrichment for CKM-MED (Figure 1F, right). These results show that, *in vitro* and in purified endogenous complexes, NRs can interact with both MED and CKM-MED but show a clear preference for interaction with the CKM-bound form of mMED.

## NR and MED26 are both needed to enable CTD binding to CKM-MED

The yeast studies that detected binding of CKM-MED to upstream activating sequences reported that the form of yeast MED found at promoters lacked the CKM and instead could interact with RNA Pol II,[26,27] but a possible connection to activation was not considered. We reasoned that the transition from CKM-MED to RNA Pol II-MED could be a critical step in regulation of transcription initiation and potentially subject to activator control. Therefore, we investigated what might enable CKM-MED to interact with RNA Pol II. Again, we used CTD binding as a proxy for RNA Pol II interaction and focused on the effect of TR or VDR because of their tight binding to MED. We first tested whether MED26 would bind to immobilized CKM-MED and suffice to enable CKM-MED interaction with the CTD. We found that incubating CKM-MED with full-length recombinant MED26, recombinant CTD (rCTD), or both, resulted in interaction with neither one (Figures 2A lanes 1 through 3 and S2A). In contrast, we found that MED26 interaction with CKM-MED was observed after ligand-dependent VDR-RXR-DNA binding to CKM-MED (Figure 2A, lane 6) and that, once VDR-RXR-DNA and MED26 were bound, the CTD could also bind to CKM-MED (Figure 2A, lane 7). Unexpectedly, CTD binding did not result in displacement of the CKM but led to a 60%–70% decrease in interaction of tail subunit MED25 with cMED (see markedly weaker MED25 band in Figure 2A lane 7). We repeated the experiment using recombinant MED26 truncation mutants to determine what portions of MED26, which includes an extended IDR (residues ~98–465) interspersed between its folded N- and C-terminal domains (Figure 2B), were involved. We found that the C-terminal domain of MED26 and a partial intervening IDR were required for enabling CTD interaction with CKM-MED (Figures 2C lane 3 and S2B). The C-terminal domain alone, or the IDR alone, was not sufficient (Figure 2C, lanes 4 and 5, respectively), and the N-terminal domain was dispensable. Thus, the association of CKM-MED with the RNA Pol II CTD is NR- and MED26-dependent and leads to changes in the tail module (MED25 dissociation), despite a ~300 Å distance between the CTD interaction site and the tail (Figure 2D).

## *In vivo* effects of MED26 deletion

Our *in vitro* observation that MED26 is essential to initiate RNA Pol II interaction with MED could explain why the subunit has a wide-ranging effect on transcription. To test this, we examined the *in vivo* impact of MED26 deletion in *Med26*$^{-/-}$ CH12 B cells.[14] Both PCR and RNA-seq analysis corroborated the

Please cite this article in press as: Zhao et al., An IDR-dependent mechanism for nuclear receptor control of Mediator interaction with RNA polymerase II, Molecular Cell (2024), https://doi.org/10.1016/j.molcel.2024.06.006



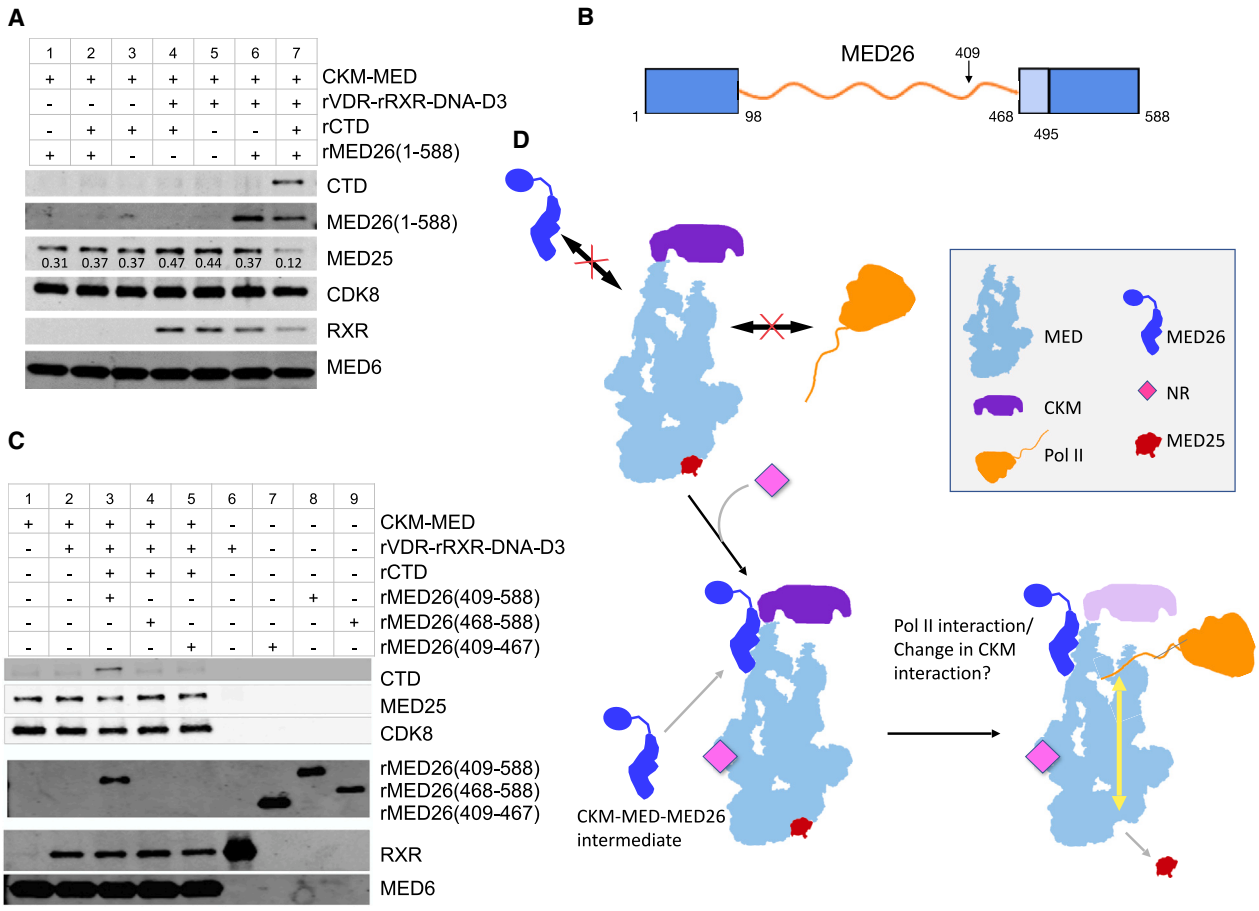


**Figure 2. NR and MED26 binding enable interaction of CKM-MED with the CTD**

(A) Western blot analysis of CKM-MED interaction with NR, rMED26, and rCTD. Recombinant MED26, CTD, assembled VDR-RXR-DNA-D3 complex, and ANTI-FLAG M2 resin were added to PC-FT, and CKM-MED complexes were pulled down through a FLAG tag on MED31. A representative gel is shown, each experiment was independently repeated three times.

(B) Domain organization of the MED26 subunit shows folded N-terminal (1–98) and C-terminal (468–588; the 495–588 portion has been identified in cryo-EM structures) domains connected by a central IDR (99–465).

(C) Western blot analysis of CKM-MED interaction with recombinant MED26 truncation deletions. Three recombinant MED26 fragments, MED26 (409–588), MED26 (468–588), and MED26 (409–467), were tested in this experiment. Each recombinant MED26 fragment, CTD, assembled VDR-RXR-DNA-D3 complex, and ANTI-FLAG M2 resin were added to PC-FT, and CKM-MED complexes were pulled down through a FLAG tag on MED31. Only the MED26 fragment, including the folded C-terminal domain and a partial IDR (aa 409–588), was able to bind to CKM-MED and enable CTD interaction in the presence of VDR-RXR-DNA-D3. The MED26 C-terminal domain alone, or the MED26 IDR alone, was not able to bind CKM-MED and enable CTD interaction. A representative gel is shown, each experiment was independently repeated three times.

(D) A diagram showing the interactions that culminate in CTD binding to CKM-MED in the presence of VDR-RXR and MED26. CTD interaction results in diminished MED25 interaction with the tail, suggesting a capacity of the cMED structure to enable allosteric control of CTD binding through changes in the tail module. See also Figure S2.

full homozygous knockout of *med26* and ruled out the presence of hypomorphic mutations or truncated MED26 isoforms.[14]

RNA-seq analysis showed an overall reduction in the transcriptome of *Med26*$^{-/-}$ cells, measured as transcript copies per cell by spike-in normalization (Figure 3A, left), and we found that RNA Pol II recruitment was considerably reduced across the genome (Figures 3A right and 3B showing profiles at the *Myc-PvtI* locus). These results are consistent with a previous report indicating reduced RNA Pol II occupancy at specific promoters after MED26 depletion.[17] Considering the dynamic binding of MED26 to the MED core (Figure 1), we next evaluated whether MED26 shows promoter-enhancer recruitment preferences compared with other MED subunits. Chromatin immunoprecipitation sequencing (ChIP-seq) analysis showed tail MED23 and MED25 subunits displaying a higher number of enhancer-associated peaks, as would be expected because there are more enhancers than promoters in the genome. In contrast, MED26 was predominantly associated with promoters (Figure 3C). For instance, at the highly active *Cd74* locus in B cells, MED23 and MED25 occupy both promoter and intragene regulatory elements, whereas MED26 is confined to promoters (Figure 3D). Notably, enhancers that were positive for MED26 showed

Please cite this article in press as: Zhao et al., An IDR-dependent mechanism for nuclear receptor control of Mediator interaction with RNA polymerase II, Molecular Cell (2024), https://doi.org/10.1016/j.molcel.2024.06.006



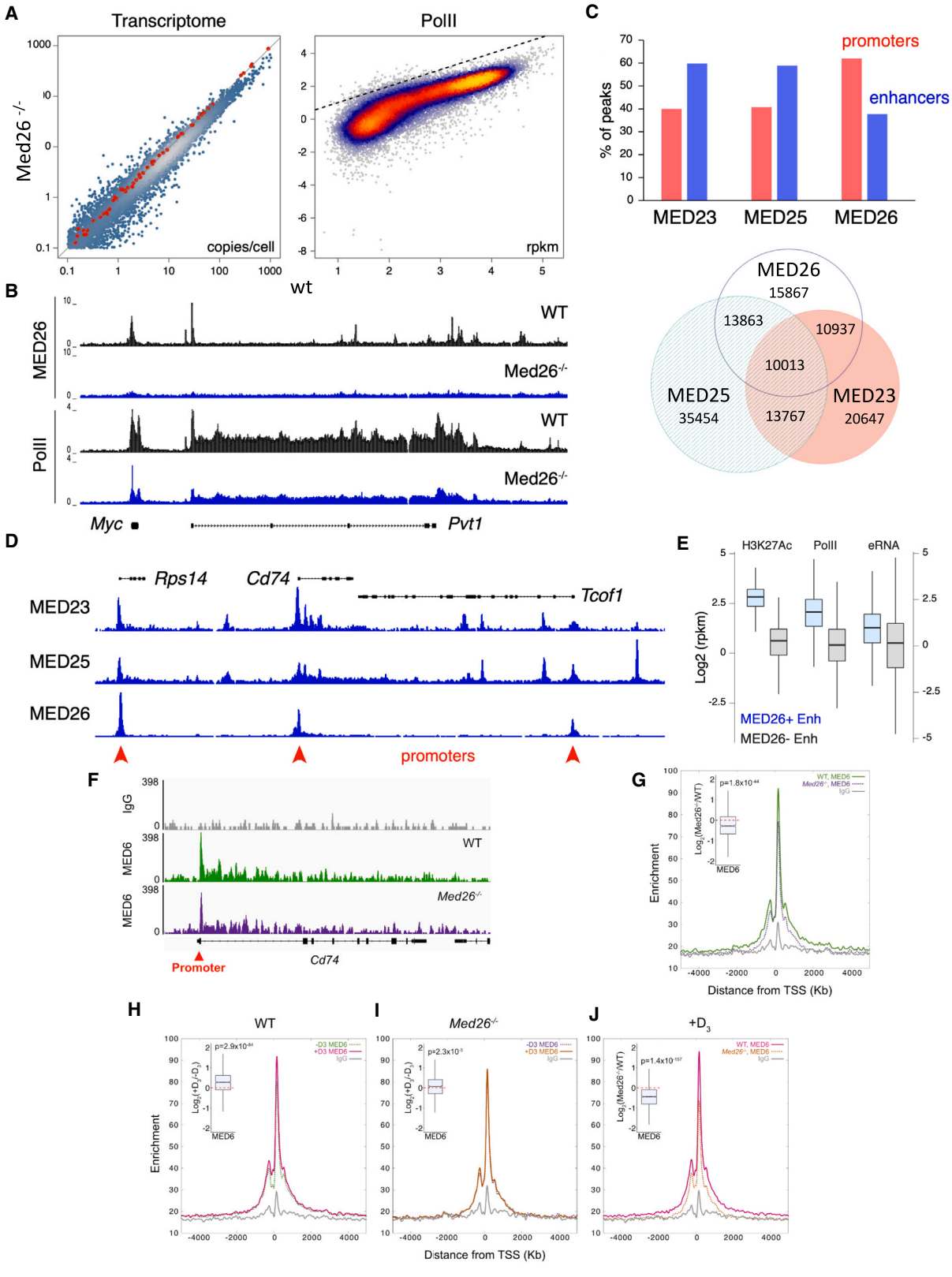


*(legend on next page)*

Please cite this article in press as: Zhao et al., An IDR-dependent mechanism for nuclear receptor control of Mediator interaction with RNA polymerase II, Molecular Cell (2024), https://doi.org/10.1016/j.molcel.2024.06.006



increased levels of RNA Pol II and RNA Pol II activity (H3K27Ac+ and eRNA+, Figure 3E) pinpointing a strong correlation between MED26 recruitment and active transcription.

To further examine the functional effects of MED26 and the subunit's role in activation by NRs *in vivo*, we carried out CUT&RUN[32] for the cMED subunit MED6 in wild-type (WT) and *Med26*$^{-/-}$ CH12 B cells, in the presence or absence of $D_3$. Consistent with the ChIP-seq data for MED23 and MED25 (see Figure 3D), we observed MED6 enrichment at both the promoter and intragene regulatory regions of the highly expressed gene *Cd74* (Figure 3F, middle). Loss of MED26 reduced MED6 signal at the *Cd74* locus (Figure 3F, bottom). We next investigated the enrichment of MED6 CUT&RUN signal relative to the transcription start sites (TSSs) of expressed genes. Correlation coefficients between two replicates for each CUT&RUN experiment were highly significant ($r = 0.74$ to $r = 0.83$; Figure S3A) and replicates for further analysis. We found that deletion of MED26 reduced MED6 signal at the TSS of expressed genes (Figure 3G), as seen for *Cd74*. This agrees with our finding of reduced transcription and reduced RNA Pol II occupancy in *Med26*$^{-/-}$ cells and is consistent with *in vivo* involvement of MED26 in facilitating RNA Pol II interaction with cMED. Treatment of WT cells with $D_3$ for 1 h resulted in increased MED6 signal at the promoters of active genes in WT cells, compared with the untreated control (Figure 3H). The $D_3$-dependent enrichment of MED6 at TSSs was blunted in the absence of MED26 (Figures 3I and 3J). The $D_3$-driven enrichment of MED6 CUT&RUN signal at TSSs and its dependence on MED26 are especially apparent if the analysis is focused on D3-induced genes (Figures S3B–S3D). Thus, complementary to our findings *in vitro*, these results demonstrate that cooperation between MED26 and NRs is essential to enable transcription activation in the cellular environment.

The presence of the MED13 ortholog, MED13L, complicated attempts to characterize the effect of the CKM in cMED interaction with RNA Pol II. Attesting to the essential and complex role of the CKM we found that, although both med13$^{-/-}$ and med13L$^{-/-}$ knockout CH12 cell lines are viable,[14] a double med13$^{-/-}$med13L$^{-/-}$ knockout in CH12 cells was synthetic lethal (Figure S3E).

## Structural basis for CKM blocking of MED26 and CTD interaction with cMED

To unravel the molecular details underlying the MED26 versus CKM competition for cMED binding, we purified CKM-MED to homogeneity and determined its structure and intermolecular interactions using cryo-EM and crosslinking-mass spectrometry (XL-MS). Image analysis and three-dimensional (3D) classification of the CKM-MED cryo-EM dataset segregated CKM-MED particles into two distinct subsets (Figure S4A). In about half the particles, cMED remained essentially unchanged. A cryo-EM map calculated from CKM-MED particles with the standard cMED conformation (Figure 4A, left) had a 4.8 Å overall resolution (Figure S4B; Table S1) and showed density matching the expected shape and location of the CKM adjacent to cMED, as seen in averages of CKM-MED images preserved in stain (e.g., Figure 1E). Considerable blurring of the CKM density indicates that its position is highly variable. A molecular model of the cMED portion of CKM-MED (Figure 4A, right; Table S2) is essentially the same as that of cMED in the absence of the CKM (the root-mean-square deviation [RMSD] between molecular models for cMED and the cMED portion of the standard CKM-MED conformation is ~3.6 Å). In the remaining CKM-MED particles, interaction with the CKM triggered an overall change in cMED conformation. A cryo-EM map of that alternative CKM-MED conformation (at 7.8 Å resolution, Figure S4C) revealed a rearrangement of the entire MED core, from the knob and CTD-binding gap, to MED1 and the tail module (Figures 4B and 4C; Videos S1 and S2). Notably, the tail adopted a structure reminiscent of a previously reported "split tail" conformation.[33]

It seemed surprising that limited, localized interaction of the CKM with the highly mobile cMED hook domain could result in changes throughout the entire cMED structure (including in the tail module, located >300 Å away from the CKM contact region). Fitting the molecular model of cMED in the CKM-MED cryo-EM map with a standard cMED conformation revealed non-cMED density at various locations around the CTD-binding gap, including along the base of the CTD-binding gap between the head and middle modules (Figure 4D, density "a"), near the location where the folded MED26 C-terminal domain interacts with

**Figure 3. *In vivo* effects of MED26 deletion**

(A) Left panel shows the transcriptome (mRNA copies/cell) of med26$^{-/-}$ versus WT CH12 cells. Samples were normalized with spike-in controls to be able to ascertain the presence of a global effect of MED26 deletion. The red dots correspond to external RNA control consortium (ERCC) spike-in controls used in the RNA-seq experiment. Right panel shows the same analysis for RNA Pol II recruitment (rpkm). Spike-in controls were not used in this experiment because values could be normalized against the background signal across the genome (dotted line).

(B) Large decreases in RNA Pol II recruitment across *Pvt1* observed in the absence of MED26.

(C) Percentage of ChIP-seq peaks that overlap with promoters or enhancers when pulling down MED23, MED25 (biotagged), or MED26. In contrast to tail subunits, which show a higher number of enhancer-associated peaks (as expected, given that there are more enhancers than promoters in the murine genome), MED26 is predominantly associated with promoters.

(D) An example of predominant promoter association of MED26 at a specific gene locus.

(E) Comparatively higher levels of RNA Pol II recruitment, enhancer RNA and H3K27 acetylation at MED26+ enhancers.

(F) IgG and MED6 CUT&RUN profiles at the *Cd74* locus in WT and *Med26*$^{-/-}$ CH12 B cells.

(G) Enrichment of 140–400 bp fragments from IgG or MED6 CUT&RUN relative to the transcription start site (TSS) of expressed genes in CH12 B cells ($n = 1,323$) shows reduced MED6 signal upon loss of MED26. Insert boxplot shows the $\log_2$ ratio of MED6 enrichment at the TSS + 300 bp in *Med26*$^{-/-}$ cells compared with WT.

(H–J) Same as (G), but for WT and *Med26*$^{-/-}$ CH12 B plus or minus 1 h $D_3$ treatment. Increased MED6 signal after D3 treatment at the TSS of expressed genes ($n = 1,831$, H) is lost after MED26 deletion ($n = 1,122$, I). (J) compares the effect of $D_3$ treatment in the enrichment of MED6 at the TSS of genes expressed in both WT and *Med26*$^{-/-}$ cells ($n = 1,739$). Quantification of the normalized enrichment of MED6 at the TSS + 300 bp for each of the conditions are shown in insert boxplots. *p* values were calculated using the Wilcoxon rank sum test.

See also Figure S3.

Please cite this article in press as: Zhao et al., An IDR-dependent mechanism for nuclear receptor control of Mediator interaction with RNA polymerase II, Molecular Cell (2024), https://doi.org/10.1016/j.molcel.2024.06.006



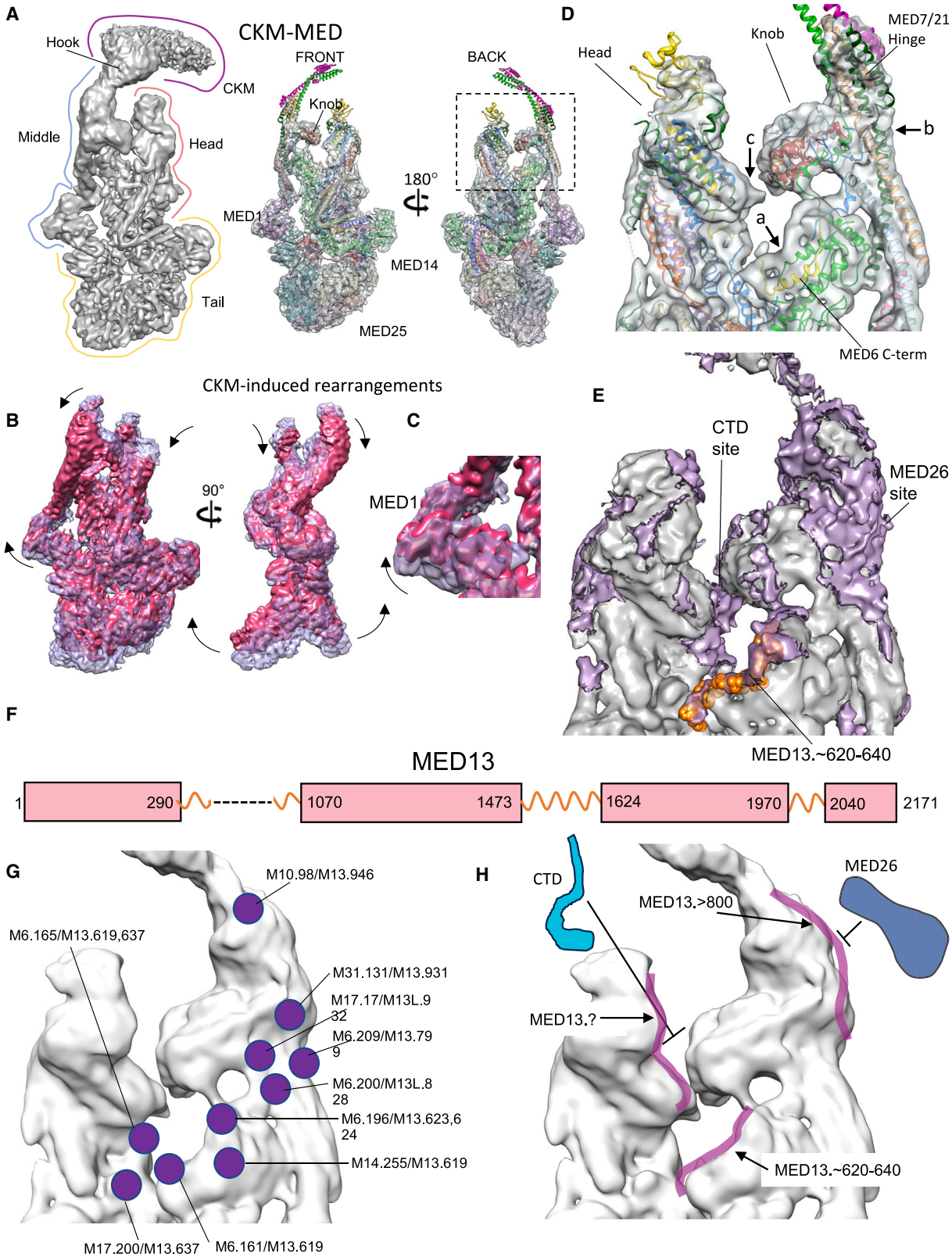


*(legend on next page)*

Please cite this article in press as: Zhao et al., An IDR-dependent mechanism for nuclear receptor control of Mediator interaction with RNA polymerase II, Molecular Cell (2024), https://doi.org/10.1016/j.molcel.2024.06.006



cMED (Figure 4D, density "b"), and around the site for CTD interaction with the head (Figure 4D, density "c"). The additional density in the cMED portion of the CKM-MED cryo-EM map was easier to recognize after segmentation based on fitting of the cMED molecular model (Figure 4E). Similar additional density could be seen after segmentation of the cryo-EM map of the alternate CKM-MED conformation (not shown). To help identify these additional densities, we conducted XL-MS analysis of CKM-MED using disuccinimidyl suberate (DSS), which specifically crosslinks proximal primary amine residues, such as lysine and protein N termini (Data S1). The observed DSS crosslinks were consistent with the known structure of cMED and with the expected organization of the mammalian CKM based on the yeast CKM structure,[34] so we focused on 16 high-confidence crosslinks between CKM and cMED subunits (Table S3A). One crosslink was mapped to the CKM contact with the hook (MED14.88-CDK19.272) and another crosslink suggested CDK8 kinase contact with MED20 (MED20.202-CDK8.119). The remaining 14 involved a large, near-N-terminal MED13 IDR (Figure 4F) crosslinking to residues in cMED subunits (Figure S4D) clustered around the CTD-binding gap and closely overlapping with observed additional density in the CKM-MED cryo-EM map (Figure 4G compare with Figure 4E). The preponderance of MED13 crosslinks over MED13L ones is likely explained by a report indicating that MED13 preferentially associates with CKM-MED, while MED13L is present in complexes that also contain MED26.[35]

The XL-MS results unequivocally point to an extensive interaction between the MED13 IDR and cMED. First, there are no crosslinks to any other CKM subunit, ruling out all but MED13 as the source of additional density in the CKM-MED cryo-EM map. Second, a multiplicity of MED6 crosslinks to other cMED subunits rules out the possibility that the clear density at the bottom of the CTD-binding gap might correspond to a disordered MED6 C terminus (Figure S4E) and, instead, identify that density as a specific portion of the MED13 IDR (residues ~620–640) that appears to have a particularly stable interaction with cMED (Figure S4F). Third, MED13 IDR interference with MED26 binding is explained by a considerable amount of partially disordered density in the CKM-MED cryo-EM map adjacent to the MED7/MED21 hinge,[36] where the well-folded MED26 C-terminal domain interacts with cMED (Figure 4E), and by two high-confidence crosslinks (MED31.131-MED13.931 and MED17.17-MED13.932) involving cMED residues located at the hinge (Figure 4G). In conclusion, an extended interaction of the MED13 IDR with cMED explains its ability to block CTD and MED26 interaction with MED and the CKM's ability to induce long-range conformational changes in cMED (Figure 4H). To further understand the effects of the MED13 interaction, we analyzed the MED26-MED and TR-hMED complexes.

## Cryo-EM and XL-MS analysis of MED26-MED

A MED26-MED cryo-EM map at 4.7 Å overall resolution (Figures S5A and S5B; Table S1) was used to refine a MED26-MED molecular model, which established that interaction with MED26 does not cause any appreciable change in cMED conformation (the RMSD between the MED26-MED and cMED molecular models was ~3.6 Å). The well-folded MED26-C-terminal domain was identified, binding at its expected location on the MED7/21 hinge (Figure 5A, MED26 C terminus ribbon model in blue), but we also observed additional density extending onto the cMED surface beyond the boundaries of the MED26 C-terminal domain, in and around the CTD-binding gap (Figure 5A, CTD shown as an atomic model in cyan [from PDB: 7ENA]). Like MED13, MED26 includes an extended (>360 residues long) central IDR (see Figure 2B) and XL-MS analysis of MED26-MED (Data S2) pointed to extensive interaction between this MED26 IDR and cMED surfaces (Table S3B), including areas around the CTD-binding gap (Figures 5B, 5C, and S5C). Notably, several cMED residues crosslink to both the MED13 and MED26 IDRs, providing evidence for their competitive interaction with cMED (Figure 5B, overlapping crosslinks marked by red circles). Of particular interest is the density at the bottom of the CTD-binding gap in the MED26-MED cryo-EM map that roughly overlaps with the location of the density in the CKM-MED map that we identified as corresponding to the MED13 IDR aa 620–640 (Figure 5D). Cryo-EM and XL-MS analyses of MED26-MED suggest that this density arises from a portion of the MED26 IDR, with its binding to cMED leading to displacement of essential MED13-cMED contacts in CKM-MED.

**Figure 4. Cryo-EM and XL-MS analysis of the CKM-MED complex**

(A) A cryo-EM map of CKM-MED with cMED in its "standard" conformation (left, map at 4.8 Å resolution) shows CKM density blurred by high mobility. On the right, two views of the cMED portion of the CKM-MED map and corresponding molecular model are shown for reference. The conformation of the cMED portion in this population of CKM-MED particles is the same as observed in the absence of the CKM.

(B) Cryo-EM map of the cMED portion of CKM-MED in its standard conformation (semi-transparent purple), compared with an alternate conformation (in solid burgundy, map resolution 7.8 Å). Curved arrows indicate the way various cMED domains are repositioned in the alternate conformation.

(C) A close-up view of the MED1 portion of the standard and alternate cMED conformations in CKM-MED.

(D) Close-up view of the CTD-binding gap portion of CKM-MED (corresponding to the area highlighted by the square in the back view shown in (A). Additional (non-cMED) well-defined density is apparent at the bottom of the gap (arrow a), next to a MED6 helix (in yellow) near the MED6 C terminus. Weaker density is also found close to the MED26 binding site (arrow b) at the MED7/MED21 hinge and on the top portion of the head near a CTD interaction patch (arrow c).

(E) Segmentation of the cMED portion of the CKM-MED map based on fitting of a cMED molecular model refined against the CKM-MED cryo-EM map shows the distribution of non-cMED density (in purple) around the CTD-binding gap. A model of MED13 IDR residues ~620–640 is shown in orange.

(F) Domain organization of CKM subunit MED13 shows folded domains separated by IDRs, particularly a very long disordered region comprising residues ~290–1,070.

(G) Crosslinks between the MED13 IDR and cMED subunits around the CTD-binding gap are marked by purple circles, with the specific residues involved indicated. Two crosslinks (MED17.413-MED13.662 and MED17.413-MED13L.673) are below the bottom of the figure and are shown in Figure 6D.

(H) A diagram illustrating how MED13 IDR (represented by purple lines) interaction with surfaces around the CTD-binding gap and the MED26 binding site would block CTD and MED26 binding to the cMED portion of the CKM-MED complex. See also Figure S4.

Please cite this article in press as: Zhao et al., An IDR-dependent mechanism for nuclear receptor control of Mediator interaction with RNA polymerase II, Molecular Cell (2024), https://doi.org/10.1016/j.molcel.2024.06.006



CellPress

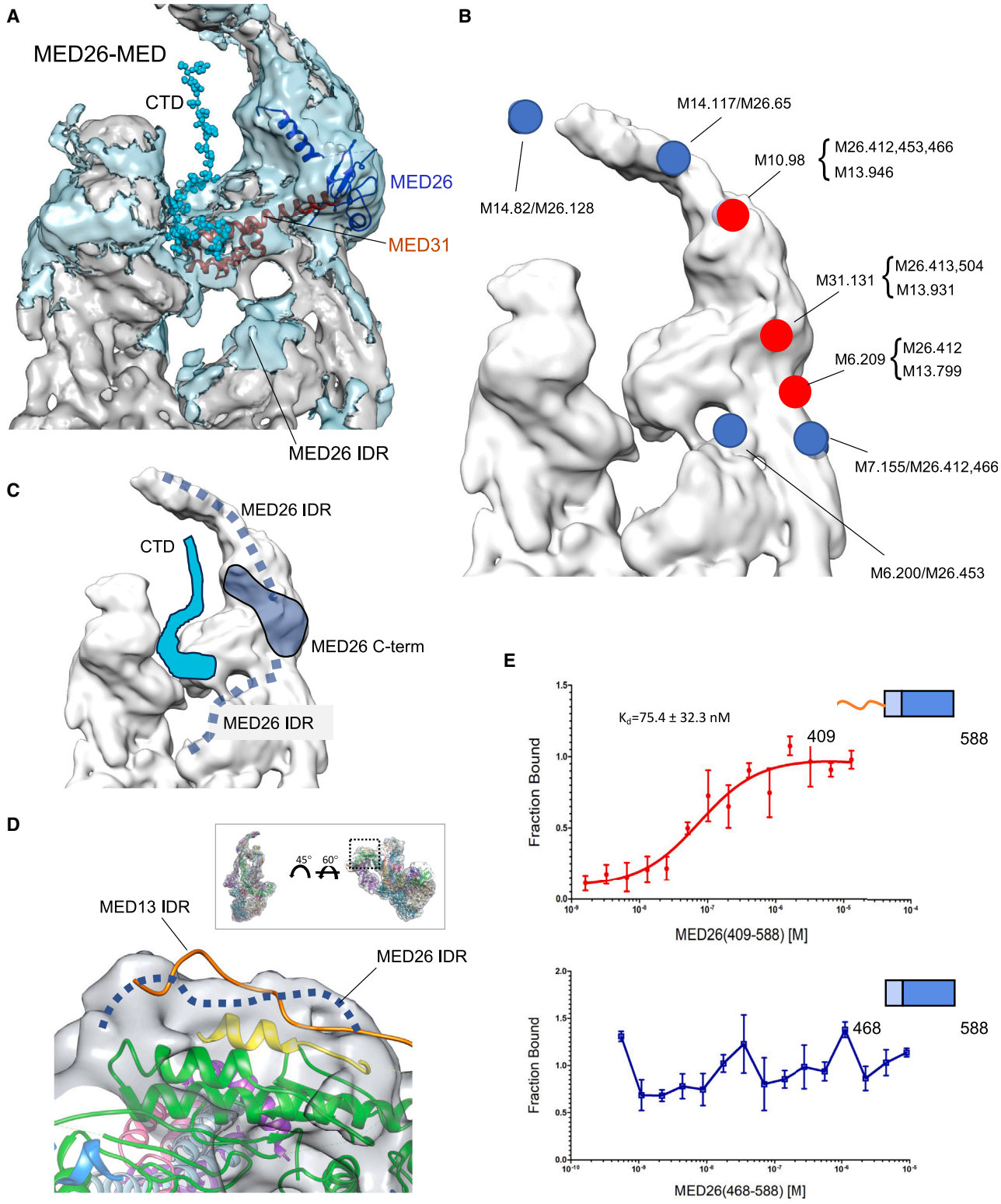


**Figure 5. MED26 interaction with cMED**

(A) Segmentation of the cMED portion of the MED26-MED map, based on fitting of a refined cMED molecular model shows non-cMED density (in light blue) corresponding to MED26, as well as along the base of the CTD-binding gap and near areas of the head involved in CTD interaction.

*(legend continued on next page)*

Please cite this article in press as: Zhao et al., An IDR-dependent mechanism for nuclear receptor control of Mediator interaction with RNA polymerase II, Molecular Cell (2024), https://doi.org/10.1016/j.molcel.2024.06.006



To investigate the role of the MED26 IDR in enabling VDR-RXR-DNA-dependent interaction of MED26 with CKM-MED, we used microscale thermophoresis. We found that the MED26 IDR is essential for stable MED26 interaction (Figure 5E, top), which is not observed with the MED26 C-terminal domain alone (Figure 5E, bottom). These findings indicate that the requirement for MED26 in enabling CTD interaction with CKM-MED relates to its IDR's role in displacing the CKM from cMED and making CTD-interacting surfaces available. Consistent with that idea, while MED26 is dispensable in *in vitro* transcription assays using a defined system with purified general factors and a head + middle + MED14 MED reconstituted from recombinant subunits, MED26 is essential to overcome the effect of a "negative cofactor" and support transcription in assays in which head + middle + MED14 are combined with CKM-containing MED-depleted nuclear extracts.[37]

The complex consequences of MED26 interaction with cMED are evidenced by an additional feature of the MED26-MED cryo-EM map: the overall structure of the highly conserved MED31 subunit, and of the entire knob domain (which is critically involved in CTD contacts), is better defined than in the cMED (substoichiometric in MED26; EMD 21514) or CKM-MED maps (Figure S6A). Therefore, we investigated how disruption of MED26-MED31 contacts might affect cMED structure and interactions.

## cMED-RNA Pol II interaction is influenced by CTD-binding gap conformation

In the cryo-EM map of MED26-MED, a helix near the MED31 C terminus (MED31 107–122) becomes ordered through contacts with 8 highly conserved MED26 C-terminal residues (MED26 593–600) that are essential for interaction with RNA Pol II[17] (Figure 6A). Results from our XL-MS analysis of CKM-MED show that the MED31 C terminus also interacts with the CKM but that interaction does not induce ordering of the knob. Although the resolution of the CKM-MED (standard conformation) and MED26-MED maps is effectively the same (~4.8 Å), the model-to-map cross-correlation for MED31 is 0.75 in MED26-MED, but only 0.68 in CKM-MED (Figure S6A).

To test the impact of MED31 C terminus interaction with MED26, we used MudPIT analysis and imaging of MED particles preserved in stain to measure the effect of MED31 C-terminal truncations. We found that deletion of 7 C-terminal residues (MED31 124–131) not resolved in cryo-EM maps had little to no effect on cMED interaction with MED26 and the CKM but caused a ~30% decrease in CTD interaction (Figures 6B and 6C left). A larger deletion (MED31 117–131) encompassing the MED31 helix that becomes ordered in MED26-MED also had a limited effect on cMED interaction with MED26 or the CKM (both establish extended, IDR-mediated interactions with cMED), but caused a further ~35% decrease in CTD binding (Figures 6B and 6C left). EM analysis revealed that this decrease in CTD binding, despite mostly unchanged MED26 interaction, resulted from reorganization of the CTD-binding gap: the larger MED31 C-terminal truncation destabilized the position of the middle module, which moved away from the head in many MED particles (Figure 6C right). A similar destabilization of the middle module, which also resulted in a marked decrease in RNA Pol II interaction, was observed in yeast MED upon deletion of five MED21 N-terminal residues located near the MED31 C terminus.[38]

Structures of yeast and human PICs indicate that the CTD establishes interactions with the CTD-binding gap formed by the head and middle modules.[39] We now show that MED26 stabilizes the CTD-binding gap through contacts with MED31 and that disruption of the binding gap leads to a decrease in cMED interaction with RNA Pol II. These results suggest that, besides exerting a direct, negative effect on cMED interaction with the CTD by blocking MED26 and CTD-binding sites, the CKM might also inhibit CTD interaction by altering the CTD-binding gap conformation of CKM-MED particles (see Figures 4B and 4C) in a way that disfavors CTD interaction.

## CKM and MED26 have different effects on the organization of cMED IDRs

Many studies have established the important role of IDR-driven phase separation in transcription regulation.[40–42] The results presented here show that partially structured IDRs in MED subunits can also directly influence intermolecular interactions, as exemplified by the effect of competitive binding of the MED13 and MED26 IDRs to cMED. We have obtained evidence that IDR behavior might also help explain preferential targeting of CKM-MED by NRs and, perhaps, other activators. We used difference mapping to highlight differences between the MED26-MED cryo-EM map and the CKM-MED cryo-EM map calculated from CKM-MED particles in which the cMED conformation is not altered. After low-pass filtering to eliminate high-frequency noise, a [CKM-MED] − [MED26-MED] difference map is remarkably clean and highlights density arising from lesser-ordered components of the complexes. The difference map shows negative MED26 density (there is no MED26 in CKM-MED), positive MED25 density (MED26-MED is substoichiometric on MED25

(B) Crosslinks between MED26 and cMED subunits around the CTD-binding gap and the hook, including crosslinks involving the MED26 IDR, are marked by light blue circles, with the specific residues involved indicated. Red circles mark the position of cMED residues that crosslink to both MED26 and the MED13 IDR, as indicated.

(C) A diagram illustrating the position of the well-folded MED26 C-terminal domain, bound at the MED7/MED21 hinge across from the CTD interaction site. The possible distribution of MED26 IDR density suggested by cryo-EM and XL-MS data is indicated by the dashed light blue lines.

(D) The MED26-MED cryo-EM map shows extra density at the base of the CTD-binding gap that partially overlaps the position observed for a portion of the MED13 IDR in the CKM-MED map.

(E) Microscale thermophoresis analysis of the interaction of MED26 truncation mutants with CKM-MED in the presence of VDR-RXR-DNA-D3. A MED26 construct (409–588), including the C-terminal domain and a partial IDR, interacts with the CKM-MED-VDR-RXR-DNA-D3 complex (top) in a dose-dependent manner. In contrast, the MED26 C terminus alone (468–588) does not bind to the CKM-MED-VDR-RXR-DNA-D3 complex (bottom), indicating that, at a minimum, a portion of the MED26 IDR is required for interaction of the subunit with CKM-MED, enabled by VDR-RXR-DNA-D3. Results are averages of three independent replicates. See also Figure S5.

Please cite this article in press as: Zhao et al., An IDR-dependent mechanism for nuclear receptor control of Mediator interaction with RNA polymerase II, Molecular Cell (2024), https://doi.org/10.1016/j.molcel.2024.06.006



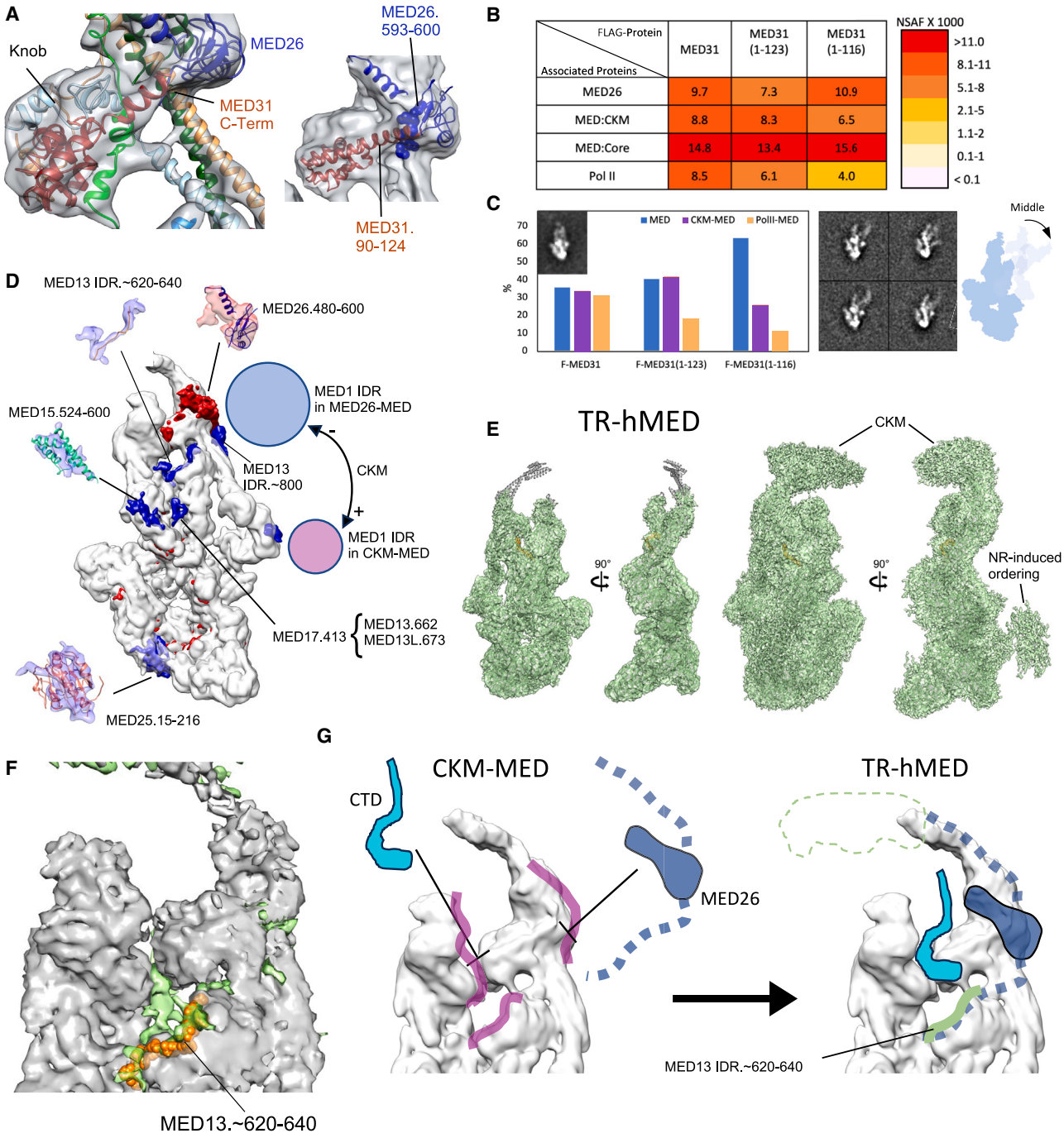


**Figure 6. Cryo-EM analysis of alternate conformation CKM-MED complex and of TR-hMED**

(A) Knob portion of the MED26-MED cryo-EM map with fitted models of component subunits. The inset shows the close interaction between the MED31 C terminus (MED31 in firebrick orange) and MED26 (in blue).

(B) MudPIT results from analysis of MEDs bearing a shorter (residues 124–131) or longer (residues 117–131) truncation of the MED31 C terminus. cMED interactions with MED26, the CKM, and RNA Pol II are largely unchanged by the shorter truncation. Deletion of a longer portion of the MED31 C terminus leaves MED26 and CKM interactions mostly unchanged but leads to a marked decrease in cMED interaction with RNA Pol II.

(C) Results from EM analysis in stain of the same MED31 truncation variants agree with the MudPIT results (a larger decrease in RNA Pol II-MED particles is observed in the longer deletion, left) and reveal the most likely cause for decreased cMED interaction with RNA Pol II, as a large number of class averages show very high variability in the position of the middle module (right panel with diagram in blue; compare averages to normal average shown as an inset in bar graph), which disrupts the organization of the CTD-binding gap.

*(legend continued on next page)*

Please cite this article in press as: Zhao et al., An IDR-dependent mechanism for nuclear receptor control of Mediator interaction with RNA polymerase II, Molecular Cell (2024), https://doi.org/10.1016/j.molcel.2024.06.006



but CKM-MED, purified from a FLAG-MED25 cell line, is not), and well-defined positive density for MED13 IDR residues ~620–640. These MED26, MED25 and MED13 densities serve as "internal controls" to validate density seen next to MED20. Six MED15-cMED crosslinks, secondary structure predictions, and comparison with the Alphafold[43] model for mouse MED15 (AF-A0JLMM5-F1-model_v4.PDB), indicate that the density corresponds to 4 short helices (aa ~524–600) in activator target subunit MED15, which are ordered in CKM-MED but not in MED26-MED (Figure 6D; Table S3C).

The effect of CKM binding extends to other cMED subunit IDRs. Results from our XL-MS analysis of the CKM-MED and MED26-MED complexes also point to differences in the behavior of the large (~700 aa) MED1 IDR targeted by TR, VDR. The degree of compaction and the position of the C-terminal portion of MED1 IDR differs between the CKM-MED and MED26-MED complexes. In the CKM-MED complex we detected ~20 crosslinks involving mostly the ~200 C-terminal residues of the MED1 IDR, suggesting that those residues are at least partially compacted. Two crosslinks (MED1.1364/MED1.172 and MED1.1518/MED1.46) position this partially ordered portion of the MED1 IDR near the N-terminal, well-folded portion of MED1 (Figure 6D; Table S3D). In contrast, roughly twice as many C-terminal MED1 IDR residues (~550 aa) are involved in ~50 intra-MED1 crosslinks in the MED26-MED complex. Three crosslinks between the MED1 IDR and the MED26 IDR (MED1.1518/MED26.404, MED26.453, and MED26.466) involve MED26 IDR residues that also crosslink to MED7 and MED10 (MED26.466/MED7.155 and MED26.453/MED10.98), locating the larger, partially ordered MED1 IDR segment in MED26-MED near MED26 (Figure 6D; Table S3E).

Our results point to the multifaceted effects of the MED13 IDR, which is involved in triggering long-range changes in cMED conformation (Figures 4B and 4C), blocking MED26 and CTD interaction with cMED (Figure 4H), and eliciting rearrangements in IDRs of cMED subunits targeted by transcription factors (Figure 6D). A rough estimate suggests that the MED13 IDR-related density identified in the CKM-MED cryo-EM map accounts for ~10% of the IDR's residues, suggesting that much remains to be understood about its interactions and function.

### Mechanism for activation of RNA Pol II interaction with CKM-MED by TR

We also determined a cryo-EM map of the TR-hMED complex with an overall resolution of 4.7 Å (Figures 6E, S6B, and S6C), which revealed details of TR interaction with cMED and provides insight into structural changes triggered by TR binding that help explain the receptor's capacity to enable interaction of CKM-MED with MED26 and the RNA Pol II CTD. First, as observed for CKM-MED, CKM density attached to the hook is highly mobile and only evident when the TR-hMED cryo-EM map is displayed at low threshold values (Figure 6E, right). Second, the cMED portion of the complex is seen only in the standard cMED conformation (Figure 6E, left), with no TR-hMED particles showing the alternate conformation found in over half of CKM-MED particles. Third, consistent with what was observed in 2D averages from stained VDR-RXRα-DNA-CKM-MED particles (Figure 1F), TR-RXRα-DNA interaction results in partially ordered density around the expected position of the MED1 IDR to which TR-RXRα-DNA binds (Figure 6E, right-most). Fourth, segmentation of the TR-hMED map after fitting the cMED molecular model shows that MED13 IDR densities observed around the head's CTD interaction patch and around the MED7/MED21 hinge in the CKM-MED cryo-EM map are entirely absent in the TR-hMED cryo-EM map, but the density along the bottom of the CTD-binding gap that we identified as MED13 IDR residues ~620–640 is clearly present (Figure 6F). These findings suggest that, by reverting the cMED portion of CKM-MED to its standard conformation (which is important for CTD binding; see Figures 6A–6C), or by affecting the behavior of the MED1 IDR, or both, TR binding destabilizes MED13 IDR interactions that block MED26 and CTD binding in CKM-MED, allowing them to bind (Figure 6G) and initiate the MED-RNA Pol II holoenzyme formation process prior to full CKM displacement. Further work will be needed to better understand the effects of TR interaction and to elucidate what steps following initial CTD interaction with CKM-MED lead to full displacement of the CKM.

## DISCUSSION

The work described here explored the effect that the dynamic association of MED26 and CKM has on cMED interaction with the RNA Pol II CTD. MED26 and the CKM have a mostly antagonistic interaction with MED because MED26 and a large IDR in CKM subunit MED13 target the same cMED surfaces. Using *in vitro* CTD binding as a direct proxy for monitoring early RNA Pol II interaction with purified MED26-MED and CKM-MED, we established that the former complex can interact with the CTD, while the latter cannot. Tight and stable

(D) A low-pass filtered difference between the cMED portions of the CKM-MED (standard conformation) and MED26-MED cryo-EM maps highlights differences between the two. Density for MED26 and MED25 acts as internal "controls" for the difference calculation (see main text for details). Clear density for 4 short MED15 α helices is only visible in the CKM-MED map, pointing to ordering of a portion of the MED15 IDR after cMED interaction with the CKM. Also illustrated are differences in compaction and position of the C-terminal portion of the MED1 IDR between the MED26-MED and CKM-MED complexes.

(E) Cryo-EM map of TR-hMED (4.7 Å resolution) and corresponding molecular model. 3D classification analysis showed that cMED only adopts its standard conformation in the presence of both the CKM and TR (left). Displaying the same map at lower threshold shows the highly mobile CKM and poorly ordered density around the expected position of the MED1 C-terminal IDR.

(F) Segmentation of the TR-hMED cryo-EM map based on a molecular model of its cMED portion shows extra density at the bottom of the CTD-binding gap (in light green), matching the position of the extra density found in the CKM-MED cryo-EM map (in orange). However, no additional density is observed at the MED26 binding site.

(G) A diagram illustrating differences in MED13 IDR density distribution between the CKM-MED (left, MED13 IDR density in burgundy) and TR-hMED (right, MED13 IDR density in light green) complexes and how they might explain activation of CKM-MED for interaction with MED26 (dark blue) and the RNA Pol II CTD (magenta). See also Figure S6.

interaction of NRs with MED prompted us to use them to study the effect of activator binding on CKM-MED interactions. We found that NRs favor binding to CKM-MED *in vitro* and in purified endogenous complexes and that they enable a transition from a non-CTD-interacting state of CKM-MED to one where CTD interaction can occur. Our focus on regulation of CTD interaction with CKM-MED as a critical initial step in MED interaction with RNA Pol II is conceptually different from earlier work, which focused on the mutually exclusive interaction of RNA Pol II and the CKM with cMED, without examining the initial CTD-dependent interaction or the effect of activators on it.

In addition to NR binding, MED26 is essential to enable CTD interaction with CKM-MED. Our structural and biochemical data suggest that this MED26 effect is explained by MED26-dependent displacement of the MED13 IDR and by MED26 stabilization of a CTD-binding gap arrangement conducive to CTD interaction. Although our experiments focused primarily on the effect of NRs that target the middle module subunit MED1, our observation that tail module subunit MED25 dissociates upon CTD binding to CKM-MED indicates that the cMED structure enables communication between the CTD-binding site and the tail (situated ~300 Å away). The observation that MED26 appears not to be essential in all mammalian cell types suggests the possibility that alternative, MED26-independent mechanisms could be present in some mammalian cells, and our conclusions are not directly applicable to transcription regulation in unicellular eukaryotes, which appear to lack a MED26 homolog.

Our conclusions are consistent with previous reports that suggested a role for CKM-MED in activation without explaining its origin. Early studies of TR activation revealed that TR recruits CKM-MED and pointed to a role of CKM-MED in activated, but not in basal, transcription.[44] HIF1a-dependent expression of hypoxia genes was found to depend on binding of the HIF1A transactivation domain to CKM-MED, which was observed to be essential for induced expression during hypoxia but not for basal expression under normal conditions.[45] Recent studies tracking *in vivo* interaction of PIC components with chromatin highlight our evolving understanding of the PIC assembly process.[46,47] It has been reported that MED can be found at enhancers, regardless of gene activation state.[48] Our results suggest that activators might play a critical role independent of MED recruitment, instead "activating" CKM-MED for CTD interaction in a MED26-dependent manner and, thus, controlling the start of PIC assembly (Figure 7). Activator-initiated, MED26-dependent activation of CKM-MED for CTD interaction could provide a mechanism for fast, efficient, and accurate transcription activation that would not rely on diffusion-limited MED recruitment by an activator.

### Limitations of the study

Our biochemical and structural studies focused on the effect of NRs targeting MED1 and provided evidence for allostery in the MED structure (dissociation of tail subunit MED25 upon CTD binding). However, future studies with activators targeting various tail subunits will be needed to test the generality of the mechanism we propose.

## STAR★METHODS

Detailed methods are provided in the online version of this paper and include the following:

- KEY RESOURCES TABLE
- RESOURCE AVAILABILITY
  - Lead contact
  - Materials availability
  - Data and code availability
- EXPERIMENTAL MODEL AND STUDY PARTICIPANT DETAILS
- METHOD DETAILS
  - Cell line creation and growth
  - CRISPR cas9 engineering of CH12 B cells
  - Purification of mouse MED
  - TR-hMED Purification
  - Plasmids and Production of recombinant proteins
  - CBP and GST pull-down assays
  - FLAG pull-down assays
  - Microscale thermophoresis (MST) assays
  - Western Blotting
  - MED26$^{-/-}$ *in vivo* assays
  - Chromatin immunoprecipitation sequencing (ChIP-seq)
  - Biotag ChIP-seq for MED25
  - GRO-seq
  - ChIP-seq, RNA-seq and Gro-seq data pre-processing
  - ChIP-seq and Gro-seq data processing
  - RNA-seq data processing
  - CUT&RUN experiments
  - MudPIT mass spectrometry
  - DSS Cross-linking/mass spectrometry analysis
  - CKM-MED, MED26-MED and TR-hMED cryo-EM sample preparation, data collection and cryo-EM map refinement
  - mMED cryo-EM map interpretation
  - EM imaging and analysis of stained specimens
- QUANTIFICATION AND STATISTICAL ANALYSIS
  - Cryo-EM

## SUPPLEMENTAL INFORMATION

Supplemental information can be found online at https://doi.org/10.1016/j.molcel.2024.06.006.

## ACKNOWLEDGMENTS

This work was supported by NIGMS grant R01GM067167 to F.J.A., NCI grants R01CA273709 and R01CA234575 to R.G.R., NIGMS grant R35GM137905 to Y.S., and NIGMS grant R35GM133434 and ACS grant RSG-22-026-01 to S.R. Work in R.C.'s lab was supported by the Intramural Research Programs of NIAMS. S.R. and G.M.B.V. were also supported by the RNA Bioscience Initiative at the University of Colorado School of Medicine. We thank Natacha Rochel-Guiberteau (IGBMC) for providing plasmids for expression of VDR and RXR. All cryo-EM data were collected at the CU Anschutz Cryo-EM Core Facility. The CU Anschutz Biophysics Core Facility helped with MST experiments. The CU Anschutz Flow Cytometry Shared Resource helped with cell sorting experiments, with support from a Skin Diseases Research Cores Grant (P30AR057212). The CU Anschutz Mass Spectrometry Proteomics Core Facility performed MudPIT experiments, except for MudPIT analysis of TR-hMED, carried out at the Proteomics Resource Center at The Rockefeller University (RRID:SCR_017797) using instrumentation funded by the Sohn Conferences Foundation and the Leona M. and Harry B Helmsley Charitable Trust. All CU Anschutz Core Facilities received partial support from the University of Colorado Cancer Center Support Grant (P30CA046934). S.R. is a Pew-Stewart Scholar for Cancer Research, supported by the Pew Charitable Trust and the Alexander and Margaret Stewart Trust. F.J.A. thanks Joan and Ron Conaway for interesting discussions that motivated some of the investigations reported here.

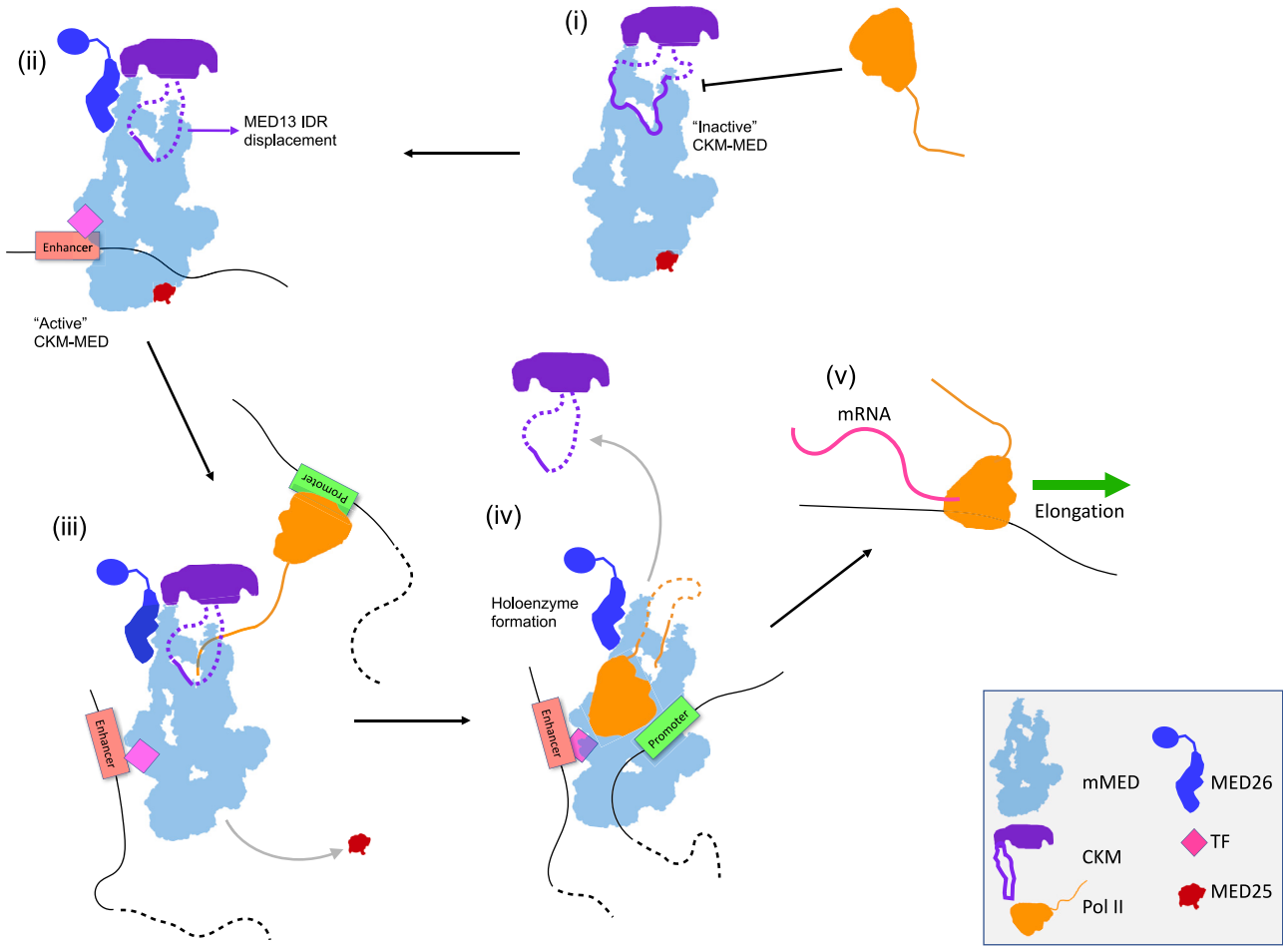


**Figure 7. Plausible steps in NR-mediated interaction of CKM-MED with RNA Pol II**

"Inactive" CKM-MED is unable to interact with RNA Pol II (step i).
Binding of an NR repositions the MED13 IDR and enables MED26 binding to CKM-MED (step ii).
RNA Pol II can interact with the "activated" CKM-MED (step iii).
Transition to a full holoenzyme complex results in release of the CKM (step iv).
Finally, RNA Pol II leaves the promoter and proceeds to elongation (step v).

## AUTHOR CONTRIBUTIONS

H.Z., J.L., R.C., Y.S., S.R., and F.J.A. designed experiments. Y.X. and Y.S. carried out XL-MS experiments. S.M. purified and biochemically characterized TR-hMED. S.V.V. performed transcriptome and ChIP-seq experiments. S.K.J. analyzed all the NGS data. J.K. generated the 3x-FLAG-MED26 CH12 cell line. A.C. generated the doubly affinity-tagged Med25$^{FLAG/FLAG}$-Med29$^{3XHA/3XHA}$ CH12 cell line. J.L. and H.Z. carried out biochemical experiments. G.M.B.V., J.L., and H.Z. carried out CUT&RUN experiments. G.M.B.V. and S.R. analyzed CUT&RUN results. H.Z. collected and analyzed EM data and generated the MED atomic models. M.R. helped interpret XL-MS results. F.J.A. wrote the manuscript.

## DECLARATION OF INTERESTS

The authors declare no competing interests.

Received: June 28, 2023
Revised: February 29, 2024
Accepted: June 7, 2024
Published: July 1, 2024

## REFERENCES

1. Soutourina, J. (2018). Transcription regulation by the Mediator complex. Nat. Rev. Mol. Cell Biol. *19*, 262–274. https://doi.org/10.1038/nrm.2017.115.

2. Malik, S., and Roeder, R.G. (2010). The metazoan Mediator co-activator complex as an integrative hub for transcriptional regulation. Nat. Rev. Genet. *11*, 761–772. https://doi.org/10.1038/nrg2901.

3. Jeronimo, C., and Robert, F. (2017). The mediator complex: at the nexus of RNA polymerase II transcription. Trends Cell Biol. *27*, 765–783. https://doi.org/10.1016/j.tcb.2017.07.001.

4. Asturias, F.J., Jiang, Y.W., Myers, L.C., Gustafsson, C.M., and Kornberg, R.D. (1999). Conserved structures of mediator and RNA polymerase II holoenzyme. Science *283*, 985–987. https://doi.org/10.1126/science.283.5404.985.

5. Verger, A., Monté, D., and Villeret, V. (2019). Twenty years of Mediator complex structural studies. Biochem. Soc. Trans. *47*, 399–410. https://doi.org/10.1042/BST20180608.

6. Tsai, K.L., Tomomori-Sato, C., Sato, S., Conaway, R.C., Conaway, J.W., and Asturias, F.J. (2014). Subunit architecture and functional modular rearrangements of the transcriptional mediator complex. Cell *157*, 1430–1444. https://doi.org/10.1016/j.cell.2014.05.015.

7. Tsai, K.L., Yu, X., Gopalan, S., Chao, T.C., Zhang, Y., Florens, L., Washburn, M.P., Murakami, K., Conaway, R.C., Conaway, J.W., and Asturias, F.J. (2017). Mediator structure and rearrangements required for holoenzyme formation. Nature *544*, 196–201. https://doi.org/10.1038/nature21393.

8. Nozawa, K., Schneider, T.R., and Cramer, P. (2017). Core Mediator structure at 3.4 A extends model of transcription initiation complex. Nature *545*, 248–251. https://doi.org/10.1038/nature22328.

9. Taatjes, D.J., Näär, A.M., Andel, F., 3rd, Nogales, E., and Tjian, R. (2002). Structure, function, and activator-induced conformations of the CRSP coactivator. Science *295*, 1058–1062. https://doi.org/10.1126/science.1065249.

10. Sato, S., Tomomori-Sato, C., Parmely, T.J., Florens, L., Zybailov, B., Swanson, S.K., Banks, C.A.S., Jin, J., Cai, Y., Washburn, M.P., et al. (2004). A set of consensus mammalian mediator subunits identified by multidimensional protein identification technology. Mol. Cell *14*, 685–691. https://doi.org/10.1016/j.molcel.2004.05.006.

11. Schilbach, S., Hantsche, M., Tegunov, D., Dienemann, C., Wigge, C., Urlaub, H., and Cramer, P. (2017). Structures of transcription pre-initiation complex with TFIIH and Mediator. Nature *551*, 204–209. https://doi.org/10.1038/nature24282.

12. Louder, R.K., He, Y., López-Blanco, J.R., Fang, J., Chacón, P., and Nogales, E. (2016). Structure of promoter-bound TFIID and model of human pre-initiation complex assembly. Nature *531*, 604–609. https://doi.org/10.1038/nature17394.

13. Murakami, K., Tsai, K.L., Kalisman, N., Bushnell, D.A., Asturias, F.J., and Kornberg, R.D. (2015). Structure of an RNA polymerase II preinitiation complex. Proc. Natl. Acad. Sci. USA *112*, 13543–13548. https://doi.org/10.1073/pnas.1518255112.

14. El Khattabi, L., Zhao, H., Kalchschmidt, J., Young, N., Jung, S., Van Blerkom, P., Kieffer-Kwon, P., Kieffer-Kwon, K.R., Park, S., Wang, X., et al. (2019). A pliable mediator acts as a functional rather than an architectural bridge between promoters and enhancers. Cell *178*, 1145–1158.e20. https://doi.org/10.1016/j.cell.2019.07.011.

15. Abdella, R., Talyzina, A., Chen, S., Inouye, C.J., Tjian, R., and He, Y. (2021). Structure of the human Mediator-bound transcription preinitiation complex. Science *372*, 52–56. https://doi.org/10.1126/science.abg3074.

16. Näär, A.M., Taatjes, D.J., Zhai, W., Nogales, E., and Tjian, R. (2002). Human CRSP interacts with RNA polymerase II CTD and adopts a specific CTD-bound conformation. Genes Dev. *16*, 1339–1344. https://doi.org/10.1101/gad.987602.

17. Takahashi, H., Parmely, T.J., Sato, S., Tomomori-Sato, C., Banks, C.A.S., Kong, S.E., Szutorisz, H., Swanson, S.K., Martin-Brown, S., Washburn, M.P., et al. (2011). Human mediator subunit MED26 functions as a docking site for transcription elongation factors. Cell *146*, 92–104. https://doi.org/10.1016/j.cell.2011.06.005.

18. Paoletti, A.C., Parmely, T.J., Tomomori-Sato, C., Sato, S., Zhu, D., Conaway, R.C., Conaway, J.W., Florens, L., and Washburn, M.P. (2006). Quantitative proteomic analysis of distinct mammalian Mediator complexes using normalized spectral abundance factors. Proc. Natl. Acad. Sci. USA *103*, 18928–18933. https://doi.org/10.1073/pnas.0606379103.

19. Malik, S., Baek, H.J., Wu, W., and Roeder, R.G. (2005). Structural and functional characterization of PC2 and RNA polymerase II-associated subpopulations of metazoan Mediator. Mol. Cell. Biol. *25*, 2117–2129. https://doi.org/10.1128/MCB.25.6.2117-2129.2005.

20. Elmlund, H., Baraznenok, V., Lindahl, M., Samuelsen, C.O., Koeck, P.J.B., Holmberg, S., Hebert, H., and Gustafsson, C.M. (2006). The cyclin-dependent kinase 8 module sterically blocks Mediator interactions with RNA polymerase II. Proc. Natl. Acad. Sci. USA *103*, 15788–15793. https://doi.org/10.1073/pnas.0607483103.

21. Knuesel, M.T., Meyer, K.D., Bernecky, C., and Taatjes, D.J. (2009). The human CDK8 subcomplex is a molecular switch that controls Mediator coactivator function. Genes Dev. *23*, 439–451. https://doi.org/10.1101/gad.1767009.

22. Tsai, K.L., Sato, S., Tomomori-Sato, C., Conaway, R.C., Conaway, J.W., and Asturias, F.J. (2013). A conserved Mediator-CDK8 kinase module association regulates Mediator-RNA polymerase II interaction. Nat. Struct. Mol. Biol. *20*, 611–619. https://doi.org/10.1038/nsmb.2549.

23. Osman, S., Mohammad, E., Lidschreiber, M., Stuetzer, A., Bazsó, F.L., Maier, K.C., Urlaub, H., and Cramer, P. (2021). The Cdk8 kinase module regulates interaction of the mediator complex with RNA polymerase II. J. Biol. Chem. *296*, 100734. https://doi.org/10.1016/j.jbc.2021.100734.

24. Myers, L.C., Gustafsson, C.M., Bushnell, D.A., Lui, M., Erdjument-Bromage, H., Tempst, P., and Kornberg, R.D. (1998). The Med proteins of yeast and their function through the RNA polymerase II carboxy-terminal domain. Genes Dev. *12*, 45–54. https://doi.org/10.1101/gad.12.1.45.

25. Davis, J.A., Takagi, Y., Kornberg, R.D., and Asturias, F.A. (2002). Structure of the yeast RNA polymerase II holoenzyme: mediator conformation and polymerase interaction. Mol. Cell *10*, 409–415. https://doi.org/10.1016/s1097-2765(02)00598-1.

26. Petrenko, N., Jin, Y., Wong, K.H., and Struhl, K. (2016). Mediator undergoes a compositional change during transcriptional activation. Mol. Cell *64*, 443–454. https://doi.org/10.1016/j.molcel.2016.09.015.

27. Jeronimo, C., Langelier, M.F., Bataille, A.R., Pascal, J.M., Pugh, B.F., and Robert, F. (2016). Tail and kinase modules differently regulate core mediator recruitment and function in vivo. Mol. Cell *64*, 455–466. https://doi.org/10.1016/j.molcel.2016.09.002.

28. Yuan, C.X., Ito, M., Fondell, J.D., Fu, Z.Y., and Roeder, R.G. (1998). The TRAP220 component of a thyroid hormone receptor- associated protein (TRAP) coactivator complex interacts directly with nuclear receptors in a ligand-dependent fashion. Proc. Natl. Acad. Sci. USA *95*, 7939–7944. https://doi.org/10.1073/pnas.95.14.7939.

29. Fondell, J.D., Ge, H., and Roeder, R.G. (1996). Ligand induction of a transcriptionally active thyroid hormone receptor coactivator complex. Proc. Natl. Acad. Sci. USA *93*, 8329–8333. https://doi.org/10.1073/pnas.93.16.8329.

30. Rachez, C., Lemon, B.D., Suldan, Z., Bromleigh, V., Gamble, M., Näär, A.M., Erdjument-Bromage, H., Tempst, P., and Freedman, L.P. (1999). Ligand-dependent transcription activation by nuclear receptors requires the DRIP complex. Nature *398*, 824–828. https://doi.org/10.1038/19783.

31. Fondell, J.D., Guermah, M., Malik, S., and Roeder, R.G. (1999). Thyroid hormone receptor-associated proteins and general positive cofactors mediate thyroid hormone receptor function in the absence of the TATA box-binding protein-associated factors of TFIID. Proc. Natl. Acad. Sci. USA *96*, 1959–1964. https://doi.org/10.1073/pnas.96.5.1959.

32. Skene, P.J., and Henikoff, S. (2017). An efficient targeted nuclease strategy for high-resolution mapping of DNA binding sites. eLife *6*, e21856. https://doi.org/10.7554/eLife.21856.

33. Chen, X., Yin, X., Li, J., Wu, Z., Qi, Y., Wang, X., Liu, W., and Xu, Y. (2021). Structures of the human Mediator and Mediator-bound preinitiation complex. Science *372*, eabg0635. https://doi.org/10.1126/science.abg0635.

34. Li, Y.C., Chao, T.C., Kim, H.J., Cholko, T., Chen, S.F., Li, G., Snyder, L., Nakanishi, K., Chang, C.E., Murakami, K., et al. (2021). Structure and non-canonical Cdk8 activation mechanism within an Argonaute-containing Mediator kinase module. Sci. Adv. *7*, eabd4484. https://doi.org/10.1126/sciadv.abd4484.

35. Daniels, D.L., F.M., Schwinn, M.K., Benink, H., Galbraith, M.D., et al. (2013). Mutual exclusivity of MED12/MED12L, MED13/13L, and CDK8/19 paralogs revealed within the CDK-mediator kinase module. J. Proteomics Bioinform. *S2*, 004. https://doi.org/10.4172/jpb.S2-004.

36. Baumli, S., Hoeppner, S., and Cramer, P. (2005). A conserved mediator hinge revealed in the structure of the MED7.MED21 (Med7.Srb7)

heterodimer. J. Biol. Chem. *280*, 18171–18178. https://doi.org/10.1074/jbc.M413466200.

37. Cevher, M.A., Shi, Y., Li, D., Chait, B.T., Malik, S., and Roeder, R.G. (2014). Reconstitution of active human core Mediator complex reveals a critical role of the MED14 subunit. Nat. Struct. Mol. Biol. *21*, 1028–1034. https://doi.org/10.1038/nsmb.2914.
38. Sato, S., Tomomori-Sato, C., Tsai, K.L., Yu, X., Sardiu, M., Saraf, A., Washburn, M.P., Florens, L., Asturias, F.J., Conaway, R.C., and Conaway, J.W. (2016). Role for the MED21-MED7 hinge in assembly of the mediator-RNA polymerase II holoenzyme. J. Biol. Chem. *291*, 26886–26898. https://doi.org/10.1074/jbc.M116.756098.
39. Schilbach, S., Wang, H., Dienemann, C., and Cramer, P. (2023). Yeast PIC-Mediator structure with RNA polymerase II C-terminal domain. Proc. Natl. Acad. Sci. USA *120*, e2220542120. https://doi.org/10.1073/pnas.2220542120.
40. Hnisz, D., Shrinivas, K., Young, R.A., Chakraborty, A.K., and Sharp, P.A. (2017). A phase separation model for transcriptional control. Cell *169*, 13–23. https://doi.org/10.1016/j.cell.2017.02.007.
41. Sabari, B.R., Dall'Agnese, A., Boija, A., Klein, I.A., Coffey, E.L., Shrinivas, K., Abraham, B.J., Hannett, N.M., Zamudio, A.V., Manteiga, J.C., et al. (2018). Coactivator condensation at super-enhancers links phase separation and gene control. Science *361*, eaar3958. https://doi.org/10.1126/science.aar3958.
42. Shrinivas, K., Sabari, B.R., Coffey, E.L., Klein, I.A., Boija, A., Zamudio, A.V., Schuijers, J., Hannett, N.M., Sharp, P.A., Young, R.A., and Chakraborty, A.K. (2019). Enhancer features that drive formation of transcriptional condensates. Mol. Cell *75*, 549–561.e7. https://doi.org/10.1016/j.molcel.2019.07.009.
43. Jumper, J., Evans, R., Pritzel, A., Green, T., Figurnov, M., Ronneberger, O., Tunyasuvunakool, K., Bates, R., Žídek, A., Potapenko, A., et al. (2021). Highly accurate protein structure prediction with AlphaFold. Nature *596*, 583–589. https://doi.org/10.1038/s41586-021-03819-2.
44. Belakavadi, M., and Fondell, J.D. (2010). Cyclin-dependent kinase 8 positively cooperates with Mediator to promote thyroid hormone receptor-dependent transcriptional activation. Mol. Cell. Biol. *30*, 2437–2448. https://doi.org/10.1128/MCB.01541-09.
45. Galbraith, M.D., Allen, M.A., Bensard, C.L., Wang, X., Schwinn, M.K., Qin, B., Long, H.W., Daniels, D.L., Hahn, W.C., Dowell, R.D., and Espinosa, J.M. (2013). HIF1A employs CDK8-mediator to stimulate RNAPII elongation in response to hypoxia. Cell *153*, 1327–1339. https://doi.org/10.1016/j.cell.2013.04.048.
46. Nguyen, V.Q., Ranjan, A., Liu, S., Tang, X., Ling, Y.H., Wisniewski, J., Mizuguchi, G., Li, K.Y., Jou, V., Zheng, Q., et al. (2021). Spatiotemporal coordination of transcription preinitiation complex assembly in live cells. Mol. Cell *81*, 3560–3575.e6. https://doi.org/10.1016/j.molcel.2021.07.022.
47. Baek, I., Friedman, L.J., Gelles, J., and Buratowski, S. (2021). Single-molecule studies reveal branched pathways for activator-dependent assembly of RNA polymerase II pre-initiation complexes. Mol. Cell *81*, 3576–3588.e6. https://doi.org/10.1016/j.molcel.2021.07.025.
48. Grünberg, S., Henikoff, S., Hahn, S., and Zentner, G.E. (2016). Mediator binding to UASs is broadly uncoupled from transcription and cooperative with TFIID recruitment to promoters. EMBO J. *35*, 2435–2446. https://doi.org/10.15252/embj.201695020.
49. Belorusova, A.Y., Bourguet, M., Hessmann, S., Chalhoub, S., Kieffer, B., Cianférani, S., and Rochel, N. (2020). Molecular determinants of MED1 interaction with the DNA bound VDR-RXR heterodimer. Nucleic Acids Res. *48*, 11199–11213. https://doi.org/10.1093/nar/gkaa775.
50. Ran, F.A., Hsu, P.D., Wright, J., Agarwala, V., Scott, D.A., and Zhang, F. (2013). Genome engineering using the CRISPR-Cas9 system. Nat. Protoc. *8*, 2281–2308. https://doi.org/10.1038/nprot.2013.143.
51. Langmead, B., and Salzberg, S.L. (2012). Fast gapped-read alignment with Bowtie 2. Nat. Methods *9*, 357–359. https://doi.org/10.1038/nmeth.1923.
52. Li, H., Handsaker, B., Wysoker, A., Fennell, T., Ruan, J., Homer, N., Marth, G., Abecasis, G., and Durbin, R.; 1000 Genome Project Data Processing Subgroup (2009). The Sequence Alignment/Map format and SAMtools. Bioinformatics *25*, 2078–2079. https://doi.org/10.1093/bioinformatics/btp352.
53. Quinlan, A.R., and Hall, I.M. (2010). BEDTools: a flexible suite of utilities for comparing genomic features. Bioinformatics *26*, 841–842. https://doi.org/10.1093/bioinformatics/btq033.
54. Chen, Z.L., Meng, J.M., Cao, Y., Yin, J.L., Fang, R.Q., Fan, S.B., Liu, C., Zeng, W.F., Ding, Y.H., Tan, D., et al. (2019). A high-speed search engine pLink 2 with systematic evaluation for proteome-scale identification of cross-linked peptides. Nat. Commun. *10*, 3404. https://doi.org/10.1038/s41467-019-11337-z.
55. Schneider, C.A., Rasband, W.S., and Eliceiri, K.W. (2012). NIH Image to ImageJ: 25 years of image analysis. Nat. Methods *9*, 671–675. https://doi.org/10.1038/nmeth.2089.
56. Yang, Z., Fang, J., Chittuluru, J., Asturias, F.J., and Penczek, P.A. (2012). Iterative stable alignment and clustering of 2D transmission electron microscope images. Structure *20*, 237–247. https://doi.org/10.1016/j.str.2011.12.007.
57. Punjani, A., Rubinstein, J.L., Fleet, D.J., and Brubaker, M.A. (2017). cryoSPARC: algorithms for rapid unsupervised cryo-EM structure determination. Nat. Methods *14*, 290–296. https://doi.org/10.1038/nmeth.4169.
58. Pettersen, E.F., Goddard, T.D., Huang, C.C., Couch, G.S., Greenblatt, D.M., Meng, E.C., and Ferrin, T.E. (2004). UCSF Chimera–a visualization system for exploratory research and analysis. J. Comput. Chem. *25*, 1605–1612. https://doi.org/10.1002/jcc.20084.
59. Adams, P.D., Afonine, P.V., Bunkóczi, G., Chen, V.B., Davis, I.W., Echols, N., Headd, J.J., Hung, L.W., Kapral, G.J., Grosse-Kunstleve, R.W., et al. (2010). Phenix: a comprehensive Python-based system for macromolecular structure solution. Acta Crystallogr. D Biol. Crystallogr. *66*, 213–221. https://doi.org/10.1107/S0907444909052925.
60. Suloway, C., Pulokas, J., Fellmann, D., Cheng, A., Guerra, F., Quispe, J., Stagg, S., Potter, C.S., and Carragher, B. (2005). Automated molecular microscopy: the new Leginon system. J. Struct. Biol. *151*, 41–60. https://doi.org/10.1016/j.jsb.2005.03.010.
61. Scheres, S.H.W. (2012). RELION: implementation of a Bayesian approach to cryo-EM structure determination. J. Struct. Biol. *180*, 519–530. https://doi.org/10.1016/j.jsb.2012.09.006.
62. Emsley, P., Lohkamp, B., Scott, W.G., and Cowtan, K. (2010). Features and development of coot. Acta Crystallogr. D Biol. Crystallogr. *66*, 486–501. https://doi.org/10.1107/S0907444910007493.
63. Dignam, J.D., Martin, P.L., Shastry, B.S., and Roeder, R.G. (1983). Eukaryotic gene transcription with purified components. Methods Enzymol. *101*, 582–598. https://doi.org/10.1016/0076-6879(83)01039-3.
64. Vian, L., Pękowska, A., Rao, S.S.P., Kieffer-Kwon, K.R., Jung, S., Baranello, L., Huang, S.C., El Khattabi, L., Dose, M., Pruett, N., et al. (2018). The energetics and physiological impact of cohesin extrusion. Cell *173*, 1165–1178.e20. https://doi.org/10.1016/j.cell.2018.03.072.
65. Wu, T.D., and Nacu, S. (2010). Fast and SNP-tolerant detection of complex variants and splicing in short reads. Bioinformatics *26*, 873–881. https://doi.org/10.1093/bioinformatics/btq057.
66. Martin, M. (2011). Cutadapt removes adapter sequences from high-throughput sequencing reads. EMBnet. j. *17*, 3. https://doi.org/10.14806/ej.17.1.200.
67. Florens, L., Carozza, M.J., Swanson, S.K., Fournier, M., Coleman, M.K., Workman, J.L., and Washburn, M.P. (2006). Analyzing chromatin remodeling complexes using shotgun proteomics and normalized spectral abundance factors. Methods *40*, 303–311. https://doi.org/10.1016/j.ymeth.2006.07.028.
68. Zhang, Y., Wen, Z., Washburn, M.P., and Florens, L. (2010). Refinements to label free proteome quantitation: how to deal with peptides shared by

multiple proteins. Anal. Chem. *82*, 2272–2281. https://doi.org/10.1021/ac9023999.

69. Zybailov, B., Mosley, A.L., Sardiu, M.E., Coleman, M.K., Florens, L., and Washburn, M.P. (2006). Statistical analysis of membrane proteome expression changes in Saccharomyces cerevisiae. J. Proteome Res. *5*, 2339–2347. https://doi.org/10.1021/pr060161n.
70. Xiang, Y., Shen, Z., and Shi, Y. (2020). Chemical cross-linking and mass spectrometric analysis of the endogenous yeast exosome complexes. Methods Mol. Biol. *2062*, 383–400. https://doi.org/10.1007/978-1-4939-9822-7_18.
71. Kim, S.J., Fernandez-Martinez, J., Nudelman, I., Shi, Y., Zhang, W., Raveh, B., Herricks, T., Slaughter, B.D., Hogan, J.A., Upla, P., et al. (2018). Integrative structure and functional anatomy of a nuclear pore complex. Nature *555*, 475–482. https://doi.org/10.1038/nature26003.
72. Shi, Y., Pellarin, R., Fridy, P.C., Fernandez-Martinez, J., Thompson, M.K., Li, Y., Wang, Q.J., Sali, A., Rout, M.P., and Chait, B.T. (2015). A strategy for dissecting the architectures of native macromolecular assemblies. Nat. Methods *12*, 1135–1138. https://doi.org/10.1038/nmeth.3617.
73. Xiang, Y., Sang, Z., Bitton, L., Xu, J., Liu, Y., Schneidman-Duhovny, D., and Shi, Y. (2021). Integrative proteomics identifies thousands of distinct, multi-epitope, and high-affinity nanobodies. Cell Syst. *12*, 220–234.e9. https://doi.org/10.1016/j.cels.2021.01.003.
74. Xiang, Y., Nambulli, S., Xiao, Z., Liu, H., Sang, Z., Duprex, W.P., Schneidman-Duhovny, D., Zhang, C., and Shi, Y. (2020). Versatile and multivalent nanobodies efficiently neutralize SARS-CoV-2. Science *370*, 1479–1484. https://doi.org/10.1126/science.abe4747.
75. Shi, Y., Fernandez-Martinez, J., Tjioe, E., Pellarin, R., Kim, S.J., Williams, R., Schneidman-Duhovny, D., Sali, A., Rout, M.P., and Chait, B.T. (2014). Structural characterization by cross-linking reveals the detailed architecture of a coatomer-related heptameric module from the nuclear pore complex. Mol. Cell. Proteomics *13*, 2927–2943. https://doi.org/10.1074/mcp.M114.041673.

Please cite this article in press as: Zhao et al., An IDR-dependent mechanism for nuclear receptor control of Mediator interaction with RNA polymerase II, Molecular Cell (2024), https://doi.org/10.1016/j.molcel.2024.06.006



## STAR★METHODS

### KEY RESOURCES TABLE

| REAGENT or RESOURCE | SOURCE | IDENTIFIER |
|---|---|---|
| **Antibodies** | | |
| RNA Pol II | Santa Cruz Biotechnology | Cat# sc-56767; RRID: AB_785522 |
| MED25 | Santa Cruz Biotechnology | Cat# sc-393759; RRID: AB_3099538 |
| Cdk8 | Santa Cruz Biotechnology | Cat# sc-13155; RRID: AB_627244 |
| RXRα | Santa Cruz Biotechnology | Cat# sc-46659; RRID: AB_2184877 |
| MED13 | Cell Signaling Technology | Cat# 91684S; RRID: AB_3099540 |
| MED6 | Proteintech | Cat# 15338-1-AP; RRID: AB_2142554 |
| GST tag | Invitrogen Life Technologies | Cat# A5800; RRID: AB_2536195 |
| RNA Pol II | Abcam | Cat# ab817; RRID: AB_306327 |
| MED26 | Cell Signaling Technology | Cat# 13641S; RRID: AB_2798281 |
| MED23 | Bethyl Laboratories | Cat# A300-425A; RRID: AB_2142309 |
| H3K27Ac | Abcam | Cat# ab4729; RRID: AB_2118291 |
| RPB9 | Invitrogen Life Technologies | Cat# PA5-60938; RRID: AB_2645762 |
| MBP | Invitrogen Life Technologies | Cat# PA1-989; RRID: AB_559988 |
| IR800CW anti-mouse secondary | LI-COR Biosciences | Cat# 926-32212: RRID: AB_621847 |
| IR680RD anti-rabbit secondary | LI-COR Biosciences | Cat#: 926-68071; RRID: AB_10956166 |
| **Bacterial and virus strains** | | |
| BL21(DE3) Competent Cells | Thermo Fisher Scientific | Cat# EC0114 |
| DH5α Competent Cells | Thermo Fisher Scientific | Cat# EC0112 |
| **Chemicals, peptides, and recombinant proteins** | | |
| ERCC RNA Spike-In Mix | Thermo Fisher Scientific | Cat# 4456740 |
| pAG-MNase | Epicypher Inc. | Cat# 15-1016 |
| Fetal Bovine Serum, value | Gibco™ | Cat# A5256701 |
| β-mercaptoethanol | Gibco™ | Cat# 21985-023 |
| Charcoal stripped Fetal Bovine Serum | Gibco | Cat# 12676029 |
| Lipofectamine LTX Reagent with PLUS Reagent | Thermo Fisher Scientific | Cat# 15338100 |
| Hygromycin B | GoldBio | Cat# H-270-1 |
| Carbenicillin | GoldBio | Cat# C103-50 |
| isopropyl β-D-1-thiogalactopyranoside | GoldBio | Cat# I2481C |
| $Ni^{2+}$-agarose resin | GoldBio | Cat# H-320-5 |
| Kanamycin | GoldBio | Cat# K-120-50 |
| Penicillin-Streptomycin | Gibco™ | Cat# 31985-070 |
| RPMI medium 1640 | Gibco™ | Cat# 11875-093 |
| Formaldehyde | Sigma | Cat# 47608 |
| Glutathione Sepharose 4B resin | Cytiva | Cat# 17075601 |
| Glutathione | Alfa Aesar | Cat# J62166 |
| Purified 3xFLAG® peptide | Sigma | Cat# SAE0194 |
| FLAG® Peptide | Sigma | Cat# F3290 |
| ANTI-FLAG® M2 Affinity Gel | Sigma | Cat# A2220 |
| P11 phosphocellulose | Sigma | Cat# C2258 |
| Protease Inhibitor Cocktail | Sigma | Cat# P8340 |
| Dynabeads™ Protein A for Immunoprecipitation | Thermo Fisher Scientific | Cat# 10001D |
| Triiodothyronine ($T_3$) | Sigma | Cat# 709719 |
| RNA Fragmentation Reagents | Thermo Fisher Scientific | Cat# AM8740 |

(*Continued on next page*)

Please cite this article in press as: Zhao et al., An IDR-dependent mechanism for nuclear receptor control of Mediator interaction with RNA polymerase II, Molecular Cell (2024), https://doi.org/10.1016/j.molcel.2024.06.006





*Continued*

| REAGENT or RESOURCE | SOURCE | IDENTIFIER |
|---|---|---|
| Odyssey® blocking buffer | LI-COR | Cat# 927-70001 |
| TURBO DNase | Thermo Fisher Scientific | Cat# AM2239 |
| Proteinase K | Thermo Fisher Scientific | Cat# 4333793 |
| T4 polynucleotide kinase (PNK) | New England Biolabs | Cat# M0201S |
| Exonuclease I | New England Biolabs | Cat# M0293S |
| anti-BrdU beads | Santa Cruz Biotechnology | Cat# sc-32323 AC |
| Disuccinimidyl suberate (DSS) | Thermo Fisher Scientific | Cat# A39267 |
| HA Synthetic Peptide | Thermo Fisher Scientific | Cat# 26184 |
| Pierce™ Anti-HA Agarose | Thermo Fisher Scientific | Cat# 26181 |
| **Critical commercial assays** | | |
| SF Cell Line 4D-Nucleofector X Kit | Lonza | Cat# V4XC-2032 |
| SE Cell Line 4D-Nucleofector X Kit | Lonza | Cat# V4XC-1012 |
| DNeasy Blood & Tissue Kit | QIAGEN | Cat# 69506 |
| RNAqueous-Micro Total RNA Isolation Kit | Thermo Fisher Scientific | Cat# AM1931 |
| Zero Blunt TOPO | Thermo Fisher Scientific | Cat# K283020 |
| NEBuilder® HiFi DNA Assembly kit | New England Biolabs | Cat# E5520S |
| ChIP DNA Clean & Concentrator Kit | Zymo Research | Cat# D5205 |
| Ovation Ultralow Library System V2 | Nugen | Cat# 0344-32 |
| Mouse direct PCR kit (for genotyping) | Selleck Bioreagents | Cat# B40015 |
| Q5 High-Fidelity DNA polymerase | New England Biolabs | Cat# M0491L |
| SuperScript III First-Strand Synthesis System | Life Technologies | Cat# 18080051 |
| Superscript III reverse transcription | Life Technologies | Cat# 18080093 |
| SRSLY® PicoPlus kit | ClaretBio | Cat# CBS-K250B-24 |
| TruSeq Stranded mRNA Library Prep Kit for NeoPrep | Illumina | Cat# NP-202-1001 |
| NEBNext® Ultra™ II Directional RNA Library Prep Kit for Illumina® | New England Biolabs | Cat# E7760 |
| **Deposited data** | | |
| RNA-Seq, ChIP-Seq, GRO-Seq, and CUT&RUN data | This study | GEO: GSE233372. |
| MED26-MED | This study | EMD-40968 |
| CKM-MED-standard | This study | EMD-40971 |
| CKM-MED-alternative | This study | EMD-40975 |
| TR-hMED | This study | EMD-41107 |
| MED26-MED | This study | PDB: 8T1I |
| CKM-MED-standard | This study | PDB: 8T1L |
| TR-hMED | This study | PDB: 8T9D |
| **Experimental models: Cell lines** | | |
| CH12 B-lymphoma mouse cell line | Tasuku Honjo | N/A |
| HeLa-derived α-2 cell line | Fondel et al.[29] | N/A |
| Platinum-A (Plat-A) Retroviral Packaging Cell Line | Cell Biolabs Inc | Cat# RV-102 |
| **Oligonucleotides** | | |
| For details see Table S4 | This study | N/A |
| **Recombinant DNA** | | |
| Plasmid: pET28b-6His-VDR | Belorusova et al.[49] | N/A |
| Plasmid: pGGWA-GST-RXRαΔNTD (residues 130-462) | Belorusova et al.[49] | N/A |
| Plasmid: p0GWA-RXRαΔNTD (residues 130-462) | Belorusova et al.[49] | N/A |
| Plasmid: pcDNA3.1(+)-Hygro-3FLAG-MED31 | This study | N/A |
| Plasmid: pcDNA3.1(+)-Hygro-3FLAG-MED31 (residues 1-123) | This study | N/A |

(*Continued on next page*)

*Continued*

| REAGENT or RESOURCE | SOURCE | IDENTIFIER |
|---|---|---|
| Plasmid: pcDNA3.1(+)-Hygro-3FLAG-MED31 (residues 1-116) | This study | N/A |
| Plasmid: pSpCas9(BB)-2A-GFP (PX458) | Ran et al.[50] | Addgene, Cat# 48138 |
| Plasmid: pCR™Blunt II-TOPO™ | Thermo Fisher Scientific | Cat# 450245 |
| Plasmid: pGEX4T-GST-RPB1 CTD (residues 1467-1970) | This study | N/A |
| Plasmid: pET43a-CBP-NusA-RPB1 CTD (residues 1467-1970)-6His | This study | N/A |
| Plasmid: pET28a-GST-MED26-6His | This study | N/A |
| Plasmid: pET28a-MBP-MED26-6His | This study | N/A |
| Plasmid: pET28a-MBP-MED26 (residues 409-588)-6His | This study | N/A |
| Plasmid: pET28a-MBP-MED26 (residues 468-588)-6His | This study | N/A |
| Plasmid: pET28a-MBP-MED26 (residues 409-467)-6His | This study | N/A |
| Plasmid: pMy-biotag-MED25-T2A-mOrange | This study | N/A |
| Plasmid: pMy-BirA-T2A-EGFP | This study | N/A |
| **Software and algorithms** | | |
| Bowtie and Bowtie2 | Langmead and Salzberg[51] | bowtie2 v2.1.0 http://bowtie-bio.sourceforge.net/index.shtml |
| sgRNA online tool | N/A | https://crispr.zhaopage.com |
| Samtools | Li et al.[52] | http://samtools.sourceforge.net/ |
| Bedtools | Quinlan and Hall[53] | N/A |
| pLink2 | Chen et al.[54] | http://pfind.ict.ac.cn/software/pLink/index.html |
| ImageJ | Schneider et al.[55] | https://imagej.net/ |
| ISAC | Yang et al.[56] | https://sphire.mpg.de/wiki/doku.php?id=pipeline:isac:sxisac2 |
| cryoSPARC version 3.1 | Punjani et al.[57] | https://cryosparc.com/; RRID:SCR_016501 |
| UCSF Chimera | Pettersen et al.[58] | https://www.cgl.ucsf.edu/chimera/; RRID:SCR_004097 |
| Adobe Premier Pro | N/A | https://www.adobe.com/products/premiere.html |
| Phenix version 1.18.2 | Afonine et al.[59] | https://www.phenix-online.org/; RRID:SCR_014224 |
| Leginon | Suloway et al.[60] | https://emg.nysbc.org//projects/leginon/wiki/Leginon_Homepage |
| RELION version 3.1 | Scheres[61] | https://relion.readthedocs.io/en/release-3.1/ |
| Coot version 0.8.9.2 | Emsley et al.[62] | https://www2.mrc-lmb.cam.ac.uk/personal/ pemsley/coot/; RRID:SCR_014222 |
| AlphaFold | Jumper et al.[43] | https://alphafold.ebi.ac.uk/ |
| Prism (GraphPad) | Version 10.0.0 | www.graphpad.com |
| Scaffold | Version 4.6 | Proteome Software |
| MS Convert | Version 3.0 | ProteoWizard |
| Mascot | Version 2.5 | Matrix Science |
| **Other** | | |
| Nitrocellulose membrane | Biorad | Cat# 1620112 |

Please cite this article in press as: Zhao et al., An IDR-dependent mechanism for nuclear receptor control of Mediator interaction with RNA polymerase II, Molecular Cell (2024), https://doi.org/10.1016/j.molcel.2024.06.006



CellPress

## RESOURCE AVAILABILITY

### Lead contact

Further information and requests for resources and reagents should be directed to and will be fulfilled by the lead contact, Francisco J. Asturias (francisco.asturias@cuanschutz.edu)

### Materials availability

Plasmids and cell lines generated in this study will be available upon reasonable request from the lead contact.

### Data and code availability

- All genomic data have been deposited on the NCCBI Gene Expression Omnibus via GEO accession number GSE233372. Cryo-EM maps have been deposited at the Electron Microscopy Data Base (EMBD) and are openly available under accession codes 40968, 40971, 40975, and 41107. Atomic coordinate models derived from cryo-EM maps have been deposited at the Protein Data Bank (PDB) and are openly available under accession codes 8T1I, 8T1L, and 8T9D.
- No original code was created in this study.
- Any additional information required to reanalyze the data reported in this paper is available from the lead contact upon request.

## EXPERIMENTAL MODEL AND STUDY PARTICIPANT DETAILS

E. coli DH5α Cells were used to purify plasmids used in this study. Cells were grown overnight in Terrific Broth with antibiotics at 37°C. BL21(DE3) competent cells were used to express and purify all recombinant proteins. BL21(DE3) cells were grown in Terrific Broth with antibiotics at 37°C to an $OD_{600}$ of 0.6 and induced with 0.5 mM IPTG for at least 16 hours at 16°C for protein expression, as described in the method details below. Derived CH12 B-lymphoma mouse cell lines with FLAG or HA tags on specific mediator subunits for Mediator purification were cultured in RPMI-1640 media supplemented with 10% Fetal Bovine Serum, 1% Penicillin-Streptomycin and 50 μM β-mercaptoethanol at 37°C with 5% $CO_2$. All information about cell line creation and growth is described in the method details below. HeLa-derived α-2 cells constitutively expressing TRα were propagated in high density cultures containing bovine calf serum. The cells were induced 48 hours prior to harvesting by supplementing the culture medium with $10^{-7}$ M triiodothyronine ($T_3$). A Platinum-A retroviral packaging cell line was used to produce retroviral particles. Infectious retrovirus was harvested 48 hours post transfection.

## METHOD DETAILS

### Cell line creation and growth

In general, CH12 B cells were cultured in RPMI-1640 media (Gibco) supplemented with 10% Fetal Bovine Serum (Gibco), 1% Penicillin-Streptomycin (Gibco) and 50 μM β-mercaptoethanol (Gibco) as described previously.[14] Briefly, CH12 B cells were expanded in 2.8L baffled Fernbach flasks (PYREX™) at 37°C with 5% $CO_2$. Cells were counted, pelleted, and washed with cold PBS buffer. Nuclear extracts were prepared as described,[14] snap frozen in liquid nitrogen, and stored at -80°C. pcDNA3.1(+) plasmids encoding mouse N-terminal 3XFLAG tagged MED31 and two C-terminal truncations were generated by Genscript and transfected into CH12 B cells using the Gene Pulser Xcell Electroporation Systems (Biorad). Transfected cells were selected by treatment with 500 μg/mL hygromycin (Goldbio) and then sorted using a MA900 cell sorter (Sony). After sorting, cells were maintained in CH12 B cell growth media with 100 μg/mL hygromycin (Goldbio).

### CRISPR cas9 engineering of CH12 B cells

$MED25^{FLAG/FLAG}$ CH12 B cells have been described previously.[14] The $MED26^{FLAG/FLAG}$ CH12 B cell line was created by CRISPR/Cas9 genome editing. A homology construct to knock-in a 3XFLAG tag at the N-terminus of MED26 was amplified by PCR using the primers listed in Table S4. In a joining 'Stitch PCR' the gel purified PCR products of the 5' and 3' homology arms were amplified using the 5' homology arm forward and the 3' homology arm reverse primers. The resulting PCR product (targeting construct) was cloned into Zero Blunt TOPO (Thermo Fisher), verified by Sanger sequencing and co-transfected together with px458-Cas9-EGFP-sgRNA vector as described previously.[14] GFP+ cells were single cell sorted and genotyped to establish homozygous $MED26^{FLAG/FLAG}$ knock-in clones.

The $MED25^{FLAG/FLAG}$-$MED29^{HA/HA}$ cell line was generated by knocking-in the 3XHA tag sequence into the *med29* locus of the previously described $MED25^{FLAG/FLAG}$ CH12 B cells. sgRNAs recognizing N-terminus of *med29* were designed using the sgRNA online tool https://crispr.zhaopage.com, and one of them was cloned into the pSPCas9(BB)-2A-GFP (pX458, Addgene #48138) vector. A donor vector containing the 3XHA tag was generated by cloning 550-600 bp-long *med29* homologous arms and the 3XHA tag sequence into pCR-Blunt II-Topo vector (Thermo Fisher) using NEBuilder HiFi DNA Assembly kit (NEB). *Med29* homologous arms were amplified using gene specific primers and Q5 High Fidelity polymerase (NEB) from genomic DNA of CH12 B cells obtained by DNeasy Blood and Tissue kit (Qiagen). Silent mutations were introduced in one homologous arm to avoid Cas9/sgRNA cutting

of the donor vector. The 3XHA tag sequence was included into two of the primers used to amplify the homologous arms. The donor and sgRNA/Cas9-containing vectors were nucleofected into MED25$^{FLAG/FLAG}$ CH12 B cells using the SF Cell Line 4D-Nucleofector™ X Kit (Lonza). 48 hours post transfection, the cells were harvested and single-cell GFP positives were sorted into 96-well plates using a BD FACSAria III cell sorter (Becton Dickinson). 10-12 days post sorting, colonies were picked and genotyped to identify homozygous knock-in clones. sgRNA sequence and primers used for cloning and genotyping are listed in Table S4.

## Purification of mouse MED

In general, mouse MED was immunopurified from CH12 B cell nuclear extracts through either 3XFLAG tag or 3XHA tagging at the N-terminus of specific MED subunits as described previously.[14] Briefly, nuclear extract was incubated with either ANTI-FLAG® M2 agarose resin (Sigma) or Anti-HA agarose (Pierce) pre-equilibrated with a buffer containing 50 mM HEPES pH 7.9, 300 mM KOAc, 1mM EDTA, 10% (v/v) glycerol, 0.2%(v/v) NP40 and 1X protease inhibitor cocktail (Sigma) for at least 4 hours at 4°C with gentle shaking. This was followed by washing with a buffer containing 50 mM HEPES pH7.9, 100 mM KCl, 1mM EDTA, 5% (v/v) glycerol and 0.05% (v/v) NP40. MED was then eluted with either 500 μg/mL FLAG peptide (Sigma) or HA peptide (Pierce) in an elution buffer containing 50 mM HEPES pH7.9, 100 mM KCl, 5% (v/v) glycerol, 1 mM EDTA and 0.005% (v/v) NP40. Purified MED was snap frozen in liquid nitrogen and stored at -80°C for further analysis. To purify CKM-MED, nuclear extract was first loaded onto a P11 phosphocellulose (Whatman) column pre-equilibrated with buffer containing 20 mM HEPES pH7.9, 1.5 mM $MgCl_2$, 0.2 mM EDTA, 300 mM KCl, 10% (v/v) glycerol. The flow-through was collected and CKM-MED was then purified as described above.

## TR-hMED Purification

HeLa-derived α-2 cells,[29] which constitutively express TRα, were propagated in high density cultures containing bovine calf serum that had been stripped of ectopic hormones by passage over an anion exchange resin. The cells were induced 48 hours prior to harvesting by supplementing the culture medium with $10^{-7}$ M triiodothyronine ($T_3$). Dignam nuclear extract was prepared as described.[63] Nuclear extract (45 mL) from about $10^{10}$ cells was further processed for affinity chromatography by adjusting the salt concentration to 300 mM KCl and by addition of 0.1% (v/v) NP40 and protease inhibitors (PMSF, 0.5 mM; pepstatin 5 mg/mL, leupeptin 12.5 mg/mL). Extract was incubated with 400 μl ANTI-FLAG® M2-agarose beads (Sigma) for 12 hours at 4°C with rotation. The beads were washed 5 times, each with 6 mL of buffer containing 50 mM HEPES pH 7.9, 300 mM KCl, 20% (v/v) glycerol, 0.1 mM EDTA, 0.1% (v/v) NP40, 0.5 mM PMSF, and 2.5 mM β-mercaptoethanol. Prior to elution, beads were washed further five times, each with 1 mL of buffer containing 50 mM HEPES pH 7.9, 150 mM KCl, 5% (v/v) glycerol, 0.1 mM EDTA, and 0.005% (v/v) NP40. Step elutions were carried out by incubating the beads (with gentle rotation) in 400 μl of 0.4 mg/mL 3XFLAG peptide (Sigma) in the same buffer, first for 1 hour and two more times for 40 min each. The eluates were snap frozen in liquid nitrogen and stored at -80°C.

## Plasmids and Production of recombinant proteins

Plasmid pET28b encoding N-terminally His tagged full-length VDR (residues 1-427), pGGWA encoding N-terminally GST-tagged RXRαΔNTD (130-462), and p0GWA encoding His-tagged RXRαΔNTD (130-462) were a gift from Dr. Natacha Rochel. All primers used to construct recombinant proteins in this study are listed in Table S4. Plasmid pGEX4T encoding a C-terminally His tagged mouse Pol II RPB1 CTD (residues 1467-1970) was generated by Genscript. Plasmid pET43a encoding calmodulin binding protein (CBP)-NusA was also generated by Genscript as a backbone to create CBP-NusA fused CTD in tandem with a C-terminal His tag for purification. Plasmid pET28aGST was created by inserting DNA encoding GST and a thrombin cleavage site between *NcoI* and *NdeI* sites using plasmid pGEX4T as a template. Plasmid pET28aMalE was created similarly by inserting DNA encoding MBP and a TEV cleavage site between *NcoI* and *NdeI* sites using plasmid pMAL-c5E as a template. A mouse MED26 DNA fragment was generated by Integrated DNA Technologies (IDT) for optimal *Escherichia coli* expression and cloned into plasmids pET28aGST and pET28aMalE between *NdeI* and *XhoI* sites with a 6Xhis tag at the C-terminus. The mouse MED26 C-terminal domain with some residual IDR (residues 409-588), MED26 C-terminal domain (residues 468-588), and MED26 IDR (residues 409-467) were similarly cloned into pET28aMalE.

All plasmids expressing recombinant proteins were transformed into BL21(DE3) *E. coli* for protein production. Cells were first grown in Terrific Broth (IBI) with 100 μg/mL Carbenicillin (Goldbio) or 30 μg/mL Kanamycin (Goldbio) at 37°C to an $OD_{600}$ of 0.6, and induced with 0.5 mM isopropyl β-D-1-thiogalactopyranoside (Goldbio) for at least 16 hours at 16°C. Cells were harvested by centrifugation and resuspended in binding buffer containing 50 mM Tris-HCl pH8.0, 500 mM NaCl, 1 mM TECP, 5% (v/v) glycerol. Sonication was used to lyse the cells and the lysate was then centrifuged at 14500 rpm for 30 minutes. $Ni^{2+}$-agarose resin (GoldBio) was equilibrated with binding buffer, mixed with the supernatant for an hour at 4°C, and then loaded onto a gravity flow column. The nickel resin was washed with 5 column volumes of binding buffer and 10 column volumes of wash buffer (binding buffer included 20 mM imidazole). Protein was eluted with elution buffer (binding buffer plus 250 mM imidazole). Eluted protein fractions were pooled and dialyzed into MED elution buffer.

## CBP and GST pull-down assays

To test *in vitro* interaction of the Pol II CTD with MED26, purified CBP-NusA-CTD-$His_6$ was incubated with Calmodulin Sepharose 4B resin (GE Healthcare) pre-equilibrated with MED elution buffer supplemented with 1.5 mM $CaCl_2$ at 4°C for 1 hour. The resin was then washed 3 times with equilibration buffer. After washing the resin was mixed with purified MBP-MED26-$His_6$ at 4°C for an

Please cite this article in press as: Zhao et al., An IDR-dependent mechanism for nuclear receptor control of Mediator interaction with RNA polymerase II, Molecular Cell (2024), https://doi.org/10.1016/j.molcel.2024.06.006



hour, washed 3 times again with equilibration buffer, and then mixed with 4X SDS (Invitrogen) for SDS-PAGE and Western Blot analysis.

To test binding of VDR to various MED complexes, 3XFLAG-MED25 MED was purified as described above. A VDR-RXR-DNA-D3 complex was formed as described previously,[49] then incubated with glutathione Sepharose 4B resin (Cytiva) that had been pre-equilibrated with MED elution buffer at 4°C for 1 hour. After VDR complex binding the resin was washed 3 times with MED elution buffer, and then incubated for 4 hours at 4°C with the purified MED complex being tested. After incubation, the resin was washed 3 times, and the MED complex was eluted with elution buffer containing 20 mM glutathione (Alfa Aesar). Both the elution and the flow-through were collected for EM analysis.

### FLAG pull-down assays

To test CTD binding to MED26-MED, nuclear extract prepared from a MED26$^{FLAG/FLAG}$ CH12 B cell line and purified recombinant CTD were incubated at 4°C overnight with pre-equilibrated ANTI-FLAG® M2 agarose resin (Sigma). Afterwards, the resin was washed three times using MED elution buffer and bound complex was eluted with 500 μg/mL FLAG peptide. Eluates were analyzed by SDS-PAGE and Western Blot. To test CTD binding to CKM-MED we followed the same procedure, except that nuclear extract from a MED25$^{FLAG/FLAG}$ CH12 B cell line was run over P11 phosphocellulose prior to overnight incubation with recombinant CTD and ANTI-FLAG® M2 agarose resin.

Because we observed considerable MED25 dissociation from CKM-MED after CTD binding in the presence of VDR-RXR-DNA-D3 complex and MED26, CTD binding and related experiments that involved the VDR-RXR-DNA-D3 complex were carried out using a CH12 B cell line transfected with a pcDNA3.1(+) plasmid expressing N-terminal 3XFLAG tagged MED31. Purified recombinant proteins (CTD, wt or deletion mutant MED26, VDR-RXR-DNA-D3 complex) were mixed with prepared nuclear extract that had been passed through P11 phosphocellulose and then incubated with pre-equilibrated ANTI-FLAG® M2 agarose resin (Sigma) at 4°C overnight. The resin was then washed three times using MED elution buffer and bound complex was eluted with MED elution buffer containing 500 μg/mL FLAG peptide (Sigma). Eluates were analyzed by SDS-PAGE and Western Blot.

### Microscale thermophoresis (MST) assays

Cy5 labeled DNA was generated by IDT, and a VDR-RXR-DNA-D3 complex was prepared as described previously.[49] CKM-MED from MED25 $^{FLAG/FLAG}$ -MED29$^{HA/HA}$ cell line was prepared as described above (nuclear extract was loaded onto a P11 phosphocellulose [Whatman] column and the flow-through was collected and incubated with ANTI-FLAG® M2 agarose resin [Sigma]). After washing the immobilized CKM-MED, VDR-RXR-DNA-D3 complex was added, incubated for 4 hours, washed three times, and eluted with FLAG peptide. Two-fold serial dilutions of purified recombinant MED26(409-588) and MED26(468-588) were performed using MED elution buffer, and then mixed with CKM-MED-VDR-RXR-DNA. The mixture was then loaded onto capillary tubes, placed on a custom capillary rack and scanned using a NanoTemper Monolith NT.115 machine. Data was collected and then analyzed using Graphpad (Prism).

### Western Blotting

Samples were loaded onto a Novex™ WedgeWell™ 4-20% gel (Invitrogen), electrophoresed, blotted onto nitrocellulose membrane (Biorad), blocked with Odyssey® blocking buffer (LI-COR), and incubated with primary and secondary antibodies using standard procedures. The monoclonal anti-Pol II 8WG16 (sc-56767), anti-RXRα(sc-46659), anti-MED25(sc-393759), and anti-Cdk8(sc-13155) antibodies were from Santa Cruz. Anti-MED13 (91684S) was from Cell Signaling Technology. Polyclonal anti-MED6 (15338-1-AP) antibody was from Proteintech, anti-GST tag (A5800), anti-RPB9 (PA5-60938) and anti-MBP (PA1-989) antibodies were from Invitrogen. IRDye® 800CW donkey anti-mouse and IRDye® 680RD goat anti-rabbit secondary antibodies were both obtained from LI-COR. Blots were imaged using an Odyssey Infrared Imaging System (LI-COR) and quantified using NIH ImageJ software.

### MED26$^{-/-}$ *in vivo* assays

#### *RNA-seq*

Five hundred thousand cultured cells were harvested, pelleted and lysed in 100 mL of the Ambion RNAqueous lysis solution. RNA was extracted and treated with DNase according to manufacturer's protocol (RNAqueous-Micro Kit). ERCC RNA Spike-In Mix (ThermoFisher #4456740) was added according to manufacturer's instructions. mRNA purification, reverse transcription and library preparation were performed using either the automated Neoprep system from Illumina (TruSeq Stranded mRNA Library Prep Kit for NeoPrep) or the NEBNext Ultra II Directional RNA Library Prep Kit for Illumina (New England Biolabs). For each genotype, we sequenced at least two biological replicates except for the CH12 B Med26 knock-out, for which only a single homozygous knock-out clone was obtained. In this case, three independent sub-clones were sequenced.

### Chromatin immunoprecipitation sequencing (ChIP-seq)

Cultured cells were fixed with 1% (v/v) formaldehyde (Sigma) for 10 min at room temperature and the reaction was quenched with 125 mM glycine (Sigma). Ten million fixed cells were washed with PBS, snap-frozen and stored at -80°C until further processing. Before use, the cells were resuspended in 1 mL of RIPA buffer (10 mM Tris-HCl pH 7.6, 1 mM EDTA, 0.1% (w/v) SDS, 0.1% (w/v)

sodium deoxycholate, 1% (v/v) Triton X-100 and freshly added Complete Mini EDTA free proteinase inhibitor [Roche]). Sonication was performed using Branson Sonifier at amplitude 35%, 12 cycles of 20 second sonication followed by a 30 second pause. The chromatin was incubated for 90 min at 4°C with 40 μl of Dynabeads Protein A (or G) under rotation for pre-clearing, while 5 μg/sample of specific antibody were incubated at 4°C with 40 μl of Dynabeads Protein A (or G) and 100 μl of RIPA buffer to form antibody-Dynabeads complexes. After removing the Dynabeads used for pre-clearing, the chromatin was incubated with the specific antibody-Dynabeads complexes overnight at 4°C under slow rotation. Antibody-bound beads were washed twice with RIPA buffer, twice with RIPA buffer containing 0.3 M NaCl, twice with LiCl buffer (0.25 M LiCl, 0.5% [v/v] Igepal-630, 0.5% [w/v] sodium deoxycholate [NaDOC]), once with LiCl buffer (0.25 M LiCl, 0.5% [v/v] NP-40, 0.5% [w/v] NaDOC), once with TE pH 8.0 containing 0.2% (v/v) Triton X-100, and once with TE pH 8.0. Crosslinks were reversed by incubating the beads at 65°C for 4 hours in the presence of 0.3% (w/v) SDS and 1 mg/mL Proteinase K (Thermo Fisher Scientific). ChIP DNA was purified by ChIP DNA clean and concentrator column (Zymo research). Libraries were prepared using the Ovation Ultralow Library System V2 kit and 50-bp single-end sequencing was performed on HiSeq3000 (Illumina). Antibodies used for ChIP-seq included anti-RNA Pol II (Abcam ab817), anti-MED26 (Cell Signaling 13641S), anti-MED23 (Bethyl A300-425A) and anti-H3K27Ac (Abcam ab4729).

### Biotag ChIP-seq for MED25

*Med25* was PCR amplified with gene specific primers and Q5 High Fidelity polymerase (NEB) from cDNA of CH12 or primary activated B cells using Superscript III reverse transcription (Invitrogen). Biotag was cloned at the N-terminus of *Med25* combined with P2A-mOrange or P2AGFP by stitch PCR. Stitch PCR products were cloned into the retroviral vector pMy using restriction digestion and ligation. Retroviral particles were produced in Platinum-A retroviral packaging cell line by transfecting the clones pMy vector in presence of Lipofectamine LTX and Plus reagent (Life Technologies). Infectious retrovirus was harvested 48 hours post transfection. CH12 B cells were transduced with Vector1 (pMy-biotag-MED25-T2A-mOrange) and Vector2 (pMy-BirA-T2A-EGFP) by centrifugation for 90 min at 2500 rpm, at 32°C in the presence of 6 mg/mL polybrene. After 6 hours, cells were diluted to 0.2 million cells/mL using reconstituted RPMI medium. A second infection was performed in a similar manner. 48 hours after the second infection, B cells were harvested and GFP + mOrange double positive cells were sorted using a BD FACSAria III cell sorter (Becton Dickinson). Sorted cells (10-20 million) were activated with 1 μM retinoic acid for 4 hours, crosslinked for 10 min at 37°C with 1% (v/v) formaldehyde and quenched with 0.125 M glycine. Crosslinked cell samples were then sonicated using a Covaris sonicator to obtain DNA fragments of 200-500 bp in length. Samples were incubated with 50 mL of Dynabeads M-280 Streptavidin Beads (Invitrogen) overnight at 4°C in RIPA buffer (10 mM Tris pH 7.6, 1 mM EDTA, 0.1% [w/v] SDS, 0.1% [w/v] sodium deoxycholate and 1% [v/v] Triton X-100). Beads were washed twice with wash buffer 1 (2% [w/v] SDS), once with wash buffer 2 (0.1% [w/v] sodium deoxycholate, 1% [v/v] Triton X-100), once with wash buffer 3 (250 mM LiCl, 0.5% [v/v] NP-40, 0.5% [w/v] sodium deoxycholate, 1 mM EDTA, and 10 mM Tris-HCl pH 8.1), and then twice with TE buffer (10 mM Tris-HCl pH 7.5 and 1 mM EDTA). ChIP DNA was then extracted for 4 hours at 65°C in Tris-EDTA buffer with 0.3% (w/v) SDS and 1 mg/mL Proteinase K (Thermo Fisher Scientific). DNA was purified by ChIP DNA clean and a concentrator kit (Zymo research). Libraries were prepared using the Ovation Ultralow Library System V2 kit and 50-bp paired-end sequencing was performed on NovaSeq 6000 (Illumina). For each sample we sequenced at least two biological replicates.

### GRO-seq

Global run-on and library preparation for sequencing was performed by extracting nuclei from 20 million cells and after run-on reaction the RNA was extracted with Trizol LS Reagent (Life Technologies). RNA was treated with TURBO DNase (Life Technologies), fragmented using RNA Fragmentation Reagents (Life Technologies) and purified by running through P-30 column (Bio-Rad). The 3′ end of the fragmented RNA was dephosphorylated with T4 polynucleotide kinase (PNK; New England Biolabs) followed by heat-inactivation. Dephosphorylation reactions were purified using anti-BrdU beads (Santa Cruz) and precipitated overnight. Poly(A)-tailing and cDNA synthesis were performed the next day as described.[64] However, for reverse transcription an oligo allowing custom barcoding during final amplification was synthesized by IDT and used as listed in Table S4. After cDNA synthesis, Exonuclease I (New England Biolabs) was used to catalyze the removal of excess oligo. The DNA-RNA hybrid was purified using ChIP DNA Clean & Concentrator Kit (Zymo Research), RNaseH treated and circularized. The libraries were amplified for 11–14 cycles with oNTI201-primer and a barcode specific primer oNTI200-index as listed in Table S4. The final product was run on EX-gel (Thermo Fisher), purified and cleaned up as above.

### ChIP-seq, RNA-seq and Gro-seq data pre-processing

Reads were sequenced using the illumina HiSeq 2500, 3000 or NovaSeq 6000, following the manufacturer's instructions. The standard pipeline (CASAVA 1.8.2) was used for image analysis and base calling. Data quality was inspected with fastqc. We conducted single-end sequencing of 50-bp read-length.

### ChIP-seq and Gro-seq data processing

Sequence reads were aligned to the mouse genome (mm9) using bowtie with flags -S -m 1 -a–best– strata -n 2, and aligned reads were selected with samtools view -S -b -F4 and sorted. For Gro-seq, an additional 2 nucleotides from the 5′ end were trimmed before aligning with option '–trim5 2′. Density tracks were generated using custom software based on the samtools library to count the

number of reads in 100 bp windows normalized to window size and library size to obtain densities in units of reads per kb region per million mapped reads (rpkm) across the genome. Up to 2 redundant reads were allowed. For Gro-seq, we made strand sensitive tracks. Peaks were called by macs2 with -q 0.001 option.

### RNA-seq data processing

Reads were aligned to the mouse genome (mm9) with gsnap[65] without detecting splice junctions de novo (–novelsplicing = 0). Existing splice junctions from RefSeq annotation were taken into account (–use-splicing = /path/to/ mm9.splices.iit). Output files were filtered to remove unaligned reads and any alignments with a mapping quality less than 20. Subsequently, the same reads were also aligned to the ERCC RNA standard with bowtie with -S -m 1 -a –best –strata -n 2 options. The number of reads matching each Refseq gene was then determined using htseq-count while the number of reads matching ERCC standard RNAs was determined by a simple line count. Spike and mRNA counts were then read into R where counts were normalized by library size and exonic size of each gene to obtain RPKM (reads per kb per million aligned reads). A linear model was fit to the ERCC spike data to relate the known copy number to the measured RPKM and cell type: lm($\log_{10}$(known copy number) /$\log_{10}$(RPKM) + cell, data = counts). The linear model was then used to estimate the copy number of each expressed gene based on the cell type and measured RPKM.

### CUT&RUN experiments

For CUT&RUN experiments, MED25$^{FLAG/FLAG}$ and MED26$^{-/-}$ CH12 B cells were cultured as described above, pelleted at 1500 rpm for 5 minutes at room temperature, resuspended in growth media supplemented with 10% charcoal stripped Fetal Bovine Serum (Gibco), and expanded at 37°C with 5% $CO_2$ overnight. Prior to running all CUT&RUN experiments cells were counted and assessed for viability. For experiments involving D3-dependent activation, D3 (Sigma, prepared as 1M stock in 200 proof ethanol) was added to cells at 1 nM final concentration (ethanol only was added to controls), cells were incubated at 37°C with 5% $CO_2$ for 1 hour, and then harvested for CUT&RUN analysis.

CUT&RUN experiments were performed as previously described[32]: Five hundred thousand cells were harvested per condition and washed twice in wash buffer (20 mM HEPES pH 7.5, 150 mM NaCl, 0.5 mM spermidine and 1x protease inhibitor cocktail). Cells were bound to magnetic Concanavalin A beads for 10 min, at RT, followed by overnight incubation with primary antibody (MED6 (Proteintech, cat # 15338-1-AP) or IgG (Proteintech, cat # 15338-1-AP), 0.5 ug/sample) in antibody buffer (2 mM EDTA in Digitonin 150 buffer), at +4°C. Cells were washed twice in Digitonin buffer (20 mM HEPES pH 7.5, 150 mM NaCl, 0.5 mM spermidine, 1x protease inhibitor cocktail and 0.01% digitonin), incubated with pAG-MNase (Epicypher Inc., 1:20) in Digitonin buffer for 10 min, at RT, and washed once in Digitonin buffer. Samples were resuspended in cold Digitonin buffer containing 100mM CaCl2 and incubated for 2 hours, at +4°C, for pAG-MNase activation and chromatin digestion. Digestion was stopped by adding stop buffer (340 mM NaCl, 20 mM EDTA, 4 mM EGTA, 50 ug/ml RNase A, 50 ug/ml Glycogen) to the samples, followed by 10 min incubation at 37°C. Samples placed in magnetic rack and the supernatant containing the released chromatin fragments was collected in new tubes. SDS was added to the samples to a final concentration of 0.1% and samples were treated with 0.2 ug/ul of Proteinase K for 10 min, at 70°C. Samples were next submitted to two rounds of phenol:chloroform:isoamyl alcohol extraction (1:1) and one round of chloroform extraction (1:1). The aqueous phase was collected in new tubes and the extracted DNA was purified by binding to AMPure XP beads using a 2X ratio. CUT&RUN libraries were then prepared using the SRSLY$^{R}$ PicoPlus kit (ClaretBio) according to the manufacturer's instructions, and two biological replicates from each condition were subjected to PE150 sequencing on NovaSeq 6000 (Illumina).

#### *CUT&RUN data analysis*

CUT&RUN sequencing reads were trimmed using Cutadapt[66]: Illumina adapter sequences were removed and reads trimmed to 140 bp. Reads less than 35 bp were discarded. Trimmed reads were aligned to the mm10 version of the mouse genome using bowtie2.[51] Aligned reads were then processed from sam to bed files using Samtools[52] and Bedtools[53] and reads containing the same chromosome start and end coordinates (duplicate) were discarded from subsequent analysis. Unique reads were filtered for fragments in the range of 140 and 400 bp and used to generate wig files. CUT&RUN score in the region TSS to TSS+300 was calculated for each gene, for each condition. For each comparison, genes with CUT&RUN score >50 in at least one of the two datasets being compared were used to generate the average CUT&RUN profiles relative to the TSS. Similarly, for quantifications and statistical analysis, genes whose normalized CUT&RUN score was >50 in either of the two datasets being compared were selected. We denoted genes with at least a 2-fold increase in CUT&RUN score in the presence of $D_3$ as $D_3$-induced genes for the analysis shown in Figures S3B–S3D.

### MudPIT mass spectrometry

Identification of proteins was accomplished using multidimensional protein identification technology (MudPIT). MED complexes were digested according to the FASP protocol using a 10 kDa molecular weight cutoff filter. In brief, the samples were mixed in the filter unit with 8 M urea, 100 mM ammonium bicarbonate (AB) pH 8.0, and centrifuged at 14 000 g for 15 min. The proteins were reduced with 10 mM DTT for 30 min at RT, centrifuged, and alkylated with 55 mM iodoacetamide for 30 min at RT in the dark. Following centrifugation, samples were washed 3 times with urea solution, and 3 times with 50 mM AB, pH 8.0. Protein digestion was carried out with sequencing grade modified Trypsin (Promega) at 1/50 protease/protein (w/w) at 37°C overnight. Peptides were recovered from the filter using 50mM AB. Samples were dried in Speed-Vac and desalted and concentrated on Thermo Scientific Pierce C18 Tip.

Please cite this article in press as: Zhao et al., An IDR-dependent mechanism for nuclear receptor control of Mediator interaction with RNA polymerase II, Molecular Cell (2024), https://doi.org/10.1016/j.molcel.2024.06.006



A 20 μl of each sample was loaded onto individual Evotips for desalting and then washed with 20 μl 0.1% formic acid (FA) followed by the addition of 100 μl storage solvent (0.1% FA) to keep the Evotips wet until analysis. The Evosep One system (Evosep, Odense, Denmark) was used to separate peptides on a Pepsep column, (150 μm inter diameter, 15 cm) packed with ReproSil C18 1.9 μm, 120 Å resin. The system was coupled to the timsTOF Pro mass spectrometer (Bruker Daltonics, Bremen, Germany) via the nano-electrospray ion source (Captive Spray, Bruker Daltonics).

The mass spectrometer was operated in PASEF mode. The ramp time was set to 100 ms and 10 PASEF MS/MS scans per topN acquisition cycle were acquired. MS and MS/MS spectra were recorded from m/z 100 to 1700. The ion mobility was scanned from 0.7 to 1.50 Vs/cm$^2$. Precursors for data-dependent acquisition were isolated within ± 1 Th and fragmented with an ion mobility-dependent collision energy, which was linearly increased from 20 to 59 eV in positive mode. Low-abundance precursor ions with an intensity above a threshold of 500 counts but below a target value of 20000 counts were repeatedly scheduled and otherwise dynamically excluded for 0.4 min.

MS/MS spectra were extracted from raw data files and converted into.mgf files using MS Convert (ProteoWizard, Ver. 3.0). Peptide spectral matching was performed with Mascot (Ver. 2.5) against the Uniprot mouse database (release 201701). Mass tolerances were +/- 15 ppm for parent ions, and +/- 0.4 Da for fragment ions. Trypsin specificity was used, allowing for 1 missed cleavage. Met oxidation, Pro hydroxylation, protein N-terminal acetylation, and peptide N-terminal pyroglutamic acid formation were set as variable modifications with Cys carbamidomethylation set as a fixed modification.

Scaffold (version 4.6, Proteome Software, Portland, OR, USA) was used to validate MS/MS based peptide and protein identifications. Peptide identifications were accepted if they could be established at greater than 95.0% probability as specified by the Peptide Prophet algorithm. Protein identifications were accepted if they could be established at greater than 99.0% probability and contained at least two identified unique peptides.

To estimate relative protein levels, Normalized Spectral Abundance Factors (NSAFs) were calculated for each detected protein.[18,67–69] The NSAF is calculated as the number of spectral counts (SpC) identifying a protein, divided by the protein's length (L), divided by the sum of SpC/L for all proteins in the MudPIT run.

### DSS Cross-linking/mass spectrometry analysis

MED26-MED and CKM-MED complexes were purified from MED26$^{FLAG/FLAG}$ and MED25$^{FLAG/FLAG}$ CH12 B cell lines, respectively as described above and then buffer-exchanged into a buffer containing 50 mM HEPES pH7.9, 100 mM KCl, 1 mM EDTA,0.5 mM DTT and 0.005% (v/v) NP40 to remove extra FLAG peptide using a ZebaSpin desalting column with a 40 kDa cut-off (Thermo Scientific). Samples were then concentrated to 0.5 μM using a Vivaspin® 500 centrifugal concentrator (Sartorius). The concentrated MED complex was mixed with disuccinimidyl suberate (DSS, Thermo Scientific) to a final concentration of 0.5 mM and incubated on ice for 1 hour. The crosslinking reactions were quenched by adding 1 M Tris-HCl pH 8.0 to a final concentration of 20 mM and incubated on ice for 30 minutes.

XL-MS analysis of the MED complexes was essentially performed as previously described.[70–73] Briefly, the cross-linked complexes were in-solution digested with 1:100 (w/w) trypsin and Lys-C at 37°C overnight, with incubation with another bolus of trypsin for 4 hours to improve digestion. After proteolysis, the peptide mixtures were centrifuged, desalted and fractionated by a self-packed high pH (pH10) reverse phase resin to reduce the complexity and improve protein coverage by LC/MS. Fractionated peptides were pooled into 6 fractions, which were subsequently analyzed by a Vanquish Neo UHPLC (Thermo Fisher) coupled to an Orbitrap mass spectrometer (Exploris 480, Thermo Fisher). Briefly, cross-linked peptides were directly loaded on an analytical column (1.6 μm particle size, 100 Å pore size, 75 μm × 5 cm; IonOpticks) and eluted using a 60 min LC gradient. The Exploris 480 instrument was operated in a data-dependent mode, where the top 6 most abundant ions with a charge of +4 to +7 and above were fragmented by high-energy collisional dissociation (normalized HCD energy 30). The targeted resolution was 120,000 for MS and 30,000 for MS/MS analyses. The quadruple isolation window was 1.6 Th and the maximum injection time for MS/MS was set at 200 ms. After the MS analysis, the raw data was searched by pLink2 to identify cross-linked peptides.[54] Initial search results were obtained at 5% false discovery rate (FDR), estimated using a target-decoy search strategy. To further improve the stringency of identification, the cross-link spectra were manually verified as previously described.[70,74,75]

### CKM-MED, MED26-MED and TR-hMED cryo-EM sample preparation, data collection and cryo-EM map refinement

To prepare cryo-EM grids, purified MED26-MED was concentrated using a Vivaspin 500 centrifugal concentrator (Sartorius). For CKM-MED and TR-hMED complexes, following purification with ANTI-FLAG® M2 agarose resin (Sigma), samples were passed over a ZebaSpin Desalting column with a 40 kDa cut-off (Thermo Scientific) with MED elution buffer and concentrated to 25 μl (100-250 μg/mL). The concentrated complex was then cross-linked with 0.02% (v/v) glutaraldehyde for 10 minutes on ice. Cryo-EM samples of CKM-MED were prepared by pipetting 2.5 μL of purified complex (100-250 μg/mL) onto lacey carbon grids covered with a thin layer of continuous amorphous carbon (Ted Pella) and plasma-cleaned for 6 seconds on a Solarus plasma cleaner (Gatan) using an Ar/$O_2$ gas mixture, TR-hMED samples were prepared on holey grids (Quantifoil R1.2/1.3, EMS). Vitrification was performed in liquid ethane using a manual plunge-freeze apparatus. Cryo-EM samples were imaged on a Talos Arctica transmission electron microscope (Thermo Fisher) outfitted with an X-FEG electron source and operating at an acceleration voltage of 200 kV. Automated data collection was carried out using image-shift targeting in Leginon.[60] Images were recorded using a K3 Summit direct electron detector (Gatan). Information about imaging conditions and EM data collection statistics for MED26-MED, CKM-MED and

TR-hMED cryo-EM specimens is summarized in Table S1. We recorded zero-tilt and tilted (20-40°) images of MED26-MED cryo-EM samples to counteract the effect of an anisotropic distribution of particle orientations. Before making grids of CKM-MED and TR-hMED, we dialyzed fractions to get rid of FLAG peptide after affinity purification and that resulted in an isotropic distribution of particles orientations. Image processing was carried out using CryoSPARC.[57] Briefly, detector movie frames were subject to patch motion correction and patch CTF estimation, followed by automated template-based particle picking. Repeated rounds of 2D classification were used to clean the initial image datasets. After this initial cleaning ab-initio volume were calculated. Further rounds of 2D and 3D classification were used to obtain a final selected set of images that were used for calculation of final cryo-EM maps.

### mMED cryo-EM map interpretation

Map visualization and interpretation were done using Coot[62] for manually atomic model building, Phenix[59] for atomic model refinement, and Chimera[58] for map visualization and figure preparation. To build an atomic model of the MED26-MED, we started with the mouse MED structure (PDB ID: 6W1S) and used the MED26 and MED1 subunits from the human MED structure (PDB ID: 7EMF) as templates. The models were fitted into the overall map of MED26-MED using Chimera,[58] then manually adjusted in Coot[62] and subject to real-space refinement in Phenix.[59] The atomic model of CKM-MED was built starting from the MED26-MED model. The MED26 subunit was deleted from the model (it is not present in the CKM-MED complex). The MED19 subunit was also deleted because the CKM-MED map did not have sufficient density to fit it in the map. The ~620-640 portion of the MED13 IDR (chain 9) in the CKM-MED model was manually added using Coot[62] with poly alanines. The model was then subjected to real-space refinement using Phenix.[59] The TR-hMED cryo-EM map was refined to 4.66 Å resolution and a corresponding atomic model was built starting from the CKM-MED model. We started by fitting the CKM-MED model into the TR-hMED map using Chimera,[58] manually adjusted MED6 and the ~620–640 portion of the MED13 IDR (Chain 9) to fit into the TR-hMED map using Coot,[62] while all other subunits remained the same. The TR-hMED model was then real-space refined using Phenix.[59]

### EM imaging and analysis of stained specimens

In brief, 2.5 μl of mouse MED sample were applied onto a continuous carbon EM grid (EMS 017543) and preserved using 2% (w/v) uranyl acetate. Stained samples were imaged using a Talos L120C transmission electron microscope (Thermo-Fisher) outfitted with a $LaB_6$ filament and operating at an acceleration voltage of 120 kV. Automated data collection was carried out using Leginon,[60] with images recorded using a Ceta CMOS detector at a magnification of 36000x (corresponding to a pixel size of 3.98 Å). Particles were automatically picked from micrographs with Auto-picking in Relion,[61] using the ''Laplacian-of-Gaussian'' option to capture all MED particle images. Around 70K particle images picked for each sample type were subject to image clustering using ISAC.[56]

## QUANTIFICATION AND STATISTICAL ANALYSIS

### Cryo-EM

Global and local resolution values for cryo-EM maps (Figures S4–S6) were calculated in CryoSPARC[57] based on the Gold-standard Fourier Shell Correlation (GFSC) method with a 0.143 criterion. Refinement statistics for atomic coordinate models were calculated in Phenix.[59]